A New Approach to Model Order Reduction of the Navier-Stokes Equations

by

Maciej Balajewicz

Department of Mechanical Engineering and Materials Science
Duke University

Date: _____

Approved:

_____
Earl H. Dowell, Supervisor

_____
Laurens E. Howle

_____
Brian P. Mann

_____
Henri P. Gavin

Dissertation submitted in partial fulfillment of the requirements for the degree of Doctor of Philosophy in the Department of Mechanical Engineering and Materials Science
in the Graduate School of Duke University
2012

Abstract

(Reduced Order Modeling of Turbulent Flows)

A New Approach to Model Order Reduction of the Navier-Stokes Equations

by

Maciej Balajewicz

Department of Mechanical Engineering and Materials Science
Duke University

Date: _____

Approved:

_____
Earl H. Dowell, Supervisor

_____
Laurens E. Howle

_____
Brian P. Mann

_____
Henri P. Gavin

An abstract of a dissertation submitted in partial fulfillment of the requirements for the degree of Doctor of Philosophy in the Department of Mechanical Engineering and Materials Science
in the Graduate School of Duke University
2012

Copyright © 2012 by Maciej Balajewicz
All rights reserved except the rights granted by the
Creative Commons Attribution-Noncommercial Licence

Abstract

A new method of stabilizing low-order, proper orthogonal decomposition based reduced-order models of the Navier Stokes equations is proposed. Unlike traditional approaches, this method does not rely on empirical turbulence modeling or modification of the Navier-Stokes equations. It provides spatial basis functions different from the usual proper orthogonal decomposition basis function in that, in addition to optimally representing the solution, the new proposed basis functions also provide stable reduced-order models. The proposed approach is illustrated with two test cases: two-dimensional flow inside a square lid-driven cavity and a two-dimensional mixing layer.

To my parents, Tadeusz and Henryka Balajewicz and my brother, Greg Balajewicz.

Contents

Abstract **iv**

List of Tables **viii**

List of Figures **ix**

Acknowledgements **xiii**

1 Introduction **1**

1.1 Contribution of the present work to Model Order Reduction (MOR) . 3

1.2 Thesis outline 4

2 Methodology **6**

2.1 Spectral methods 6

2.2 Proper orthogonal decomposition (POD) 8

2.3 Projection-based ROMs of the Navier-Stokes equation 10

2.4 ROM accuracy and stability 11

3 Applications **14**

3.1 Lid-driven cavity 14

3.2 Mixing layer 17

4 Proper Orthogonal Decomposition **21**

4.1 POD basis functions of the lid-driven cavity 21

4.2 POD basis functions of the mixing layer 23

4.3 Reconstruction turbulent kinetic energy, $E(t)$ 29

4.4 Reconstruction of the full flow field, $\boldsymbol{u}(\boldsymbol{x}, t)$ 30

5 The standard POD-Galerkin MOR approach 33

5.1 Lid-driven cavity 33

5.2 Mixing layer 36

6 A new proposed stabilization approach to MOR of the Navier-Stokes equations 39

6.1 Review of stabilization approaches for linear systems 39

6.2 Review of stabilization approaches for nonlinear systems 42

6.3 A new proposed approach to stabilization of projection-based ROMs of the Navier-Stokes 45

6.4 The algorithm and numerical implementation 49

7 Stabilized Reduced Order Models (ROMs) 50

7.1 Stabilization using exact turbulent kinetic energy balance $\varepsilon' = 0$ . . . 51

7.2 Stabilization using $\varepsilon' = \varepsilon'_{stab}$ 57

7.3 Reconstruction of the full flow field 61

7.4 Robustness of stabilized ROMs to changes in Reynolds number 63

8 Conclusions 68

8.1 Summary 68

8.2 Future work 70

A Matlab code 72

A.1 Proper orthogonal decomposition 72

A.2 Numerical implementation of inner products 73

A.3 Numerical integration of Galerkin ROMs 74

A.4 Solution of the stabilization problem 75

Bibliography 79

Biography 85

List of Tables

4.1 Percent of time-averaged, turbulent kinetic energy captured by the first 250 POD basis functions of the lid-driven cavity at $\mathrm{Re_u} = 3 \times 10^4$. 22

4.2 Percent of turbulent kinetic energy captured by the first 150 POD basis functions of the mixing layer at $\mathrm{Re}_{\delta_\omega} = 500$. 26

5.1 CPU time required to generate and integrate POD-Galerkin ROMs of the lid-driven cavity. 36

5.2 CPU time required to generate and integrate POD-Galerkin ROMs of the mixing layer. 38

7.1 Percentage of turbulent kinetic energy of the lid-driven cavity captured by the first n POD basis functions vs. the first n stabilized basis functions. 52

7.2 Percentage of turbulent kinetic energy of the mixing layer captured by the first n POD basis functions vs. the first n stabilized basis functions. 57

7.3 Percentage of turbulent kinetic energy of the lid-driven cavity captured by the first n POD basis functions vs. the first n stabilized basis functions. 60

7.4 Percentage of turbulent kinetic energy of the mixing layer captured by the first n POD basis functions vs. the first n stabilized basis functions. 61

7.5 Percent error of stabilized ROMs in predicting flows at different Reynolds numbers. 66

List of Figures

3.1 Boundary conditions for the lid-driven cavity test case. 15

3.2 Vorticity contours from a DNS of the lid-driven cavity at $\mathrm{Re_u} = 3 \times 10^4$ 16

3.3 Evolution of the turbulent kinetic energy of the lid-driven cavity as predicted by the DNS: $E_{DNS}(t)$(▬). 16

3.4 Boundary conditions for mixing layer test case. 17

3.5 Vorticity contours from a DNS of the mixing at $\mathrm{Re}_{\delta_\omega} = 500$ 19

3.6 Evolution of the turbulent kinetic energy of the mixing layer as predicted by the DNS: $E_{DNS}(t)$(▬). 20

4.1 Vorticity contours of the mean mode, $\boldsymbol{u}_0(\boldsymbol{x})$ of the lid-driven cavity at $\mathrm{Re_u} = 3 \times 10^4$. 22

4.2 Vorticity contours of spatial POD basis functions of the lid-driven cavity at $\mathrm{Re_u} = 3 \times 10^4$. 24

4.3 Evolution of the temporal POD basis functions of the lid-driven cavity at $\mathrm{Re_u} = 3 \times 10^4$. 25

4.4 Vorticity contours of the mean mode, $\boldsymbol{u}_0(\boldsymbol{x})$ of the mixing layer at $\mathrm{Re}_{\delta_\omega} = 500$. 26

4.5 Vorticity contours of spatial POD basis functions of the mixing layer at $\mathrm{Re}_{\delta_\omega} = 500$. 27

4.6 Evolution of the temporal POD basis functions of the mixing layer at $\mathrm{Re}_{\delta_\omega} = 500$. 28

4.7 Reconstruction of the turbulent kinetic energy of the lid-driven cavity at $\mathrm{Re_u} = 3 \times 10^4$ using the first n POD basis functions: $n = 10$(—), $n = 20$(—) and $n = 50$(—) and compared to the DNS(▬). 29

4.8 Reconstruction of the turbulent kinetic energy of the mixing layer at $\mathrm{Re}_{\delta_\omega} = 500$ using the first n POD basis functions: $n = 10$(——), $n = 20$(——) and $n = 50$(——) and compared to the DNS(▬). 30

4.9 Reconstructions of the vorticity field of the lid-driven cavity at $t = 200$ using the first $n = 10$ and 50 POD basis functions. 31

4.10 Reconstructions of the vorticity field of the mixing layer at $t = 1000$ using the first $n = 10$ and 50 POD basis functions. 32

5.1 Evolution of the turbulent kinetic energy of the lid driven cavity as predicted by the DNS: $E_{DNS}(t)$(▬), the optimal reconstruction using the POD basis functions: $E_{OPT}(t)$(——), and the integration of a ROM derived from the standard POD-Galerkin MOR approach: $E_{ROM}(t)$(——). 35

5.2 Evolution of the turbulent kinetic energy of the mixing layer as predicted by the DNS: $E_{DNS}(t)$(▬), the optimal reconstruction using the POD basis functions: $E_{OPT}(t)$(——), and the integration of a ROM derived from the standard POD-Galerkin MOR approach: $E_{ROM}(t)$(——). 37

7.1 Evolution of the turbulent kinetic energy of the lid driven cavity as predicted by the DNS: $E_{DNS}(t)$(▬), the optimal reconstruction using the POD basis functions: $E_{OPT}(t)$(——) and the optimal reconstruction using the stabilized basis functions: $E'_{OPT}(t)$(- - -). Integration of the standard POD-Galerkin ROM: $E_{ROM}(t)$(▪▪▪) and the integration of a stabilized ROM: $E'_{ROM}(t)$(——). The stabilized ROMs are derived using an exact energy balance, $\varepsilon' = 0$ using a superposition of $N = 100$ POD basis functions. 53

7.2 Evolution of the turbulent kinetic energy of the lid driven cavity as predicted by the DNS: $E_{DNS}(t)$(▬), the optimal reconstruction using the POD basis functions: $E_{OPT}(t)$(——) and the optimal reconstruction using the stabilized basis functions: $E'_{OPT}(t)$(- - -). Integration of the standard POD-Galerkin ROM: $E_{ROM}(t)$(▪▪▪) and the integration of a stabilized ROM: $E'_{ROM}(t)$(——). The stabilized ROMs are derived using an exact energy balance, $\varepsilon' = 0$ using a superposition of $N = 100$ POD basis functions. 54

7.3 Evolution of the turbulent kinetic energy of the mixing layer as predicted by the DNS: $E_{DNS}(t)$(▬), the optimal reconstruction using the POD basis functions: $E_{OPT}(t)$(——) and the optimal reconstruction using the stabilized basis functions: $E'_{OPT}(t)$(- - -). Integration of the standard POD-Galerkin ROM: $E_{ROM}(t)$(▪▪▪) and the integration of a stabilized ROM: $E'_{ROM}(t)$(——). The stabilized ROMs are derived using an exact energy balance, $\varepsilon' = 0$ using a superposition of $N = 100$ POD basis functions. 55

7.4 Evolution of the turbulent kinetic energy of the mixing layer as predicted by the DNS: $E_{DNS}(t)$(▬), the optimal reconstruction using the POD basis functions: $E_{OPT}(t)$(——) and the optimal reconstruction using the stabilized basis functions: $E'_{OPT}(t)$(- - -). Integration of the standard POD-Galerkin ROM: $E_{ROM}(t)$(▪▪▪) and the integration of a stabilized ROM: $E'_{ROM}(t)$(——). The stabilized ROMs are derived using an exact energy balance, $\varepsilon' = 0$ using a superposition of $N = 100$ POD basis functions. 56

7.5 Evolution of the turbulent kinetic energy of the lid driven cavity as predicted by the DNS(▬), the standard POD-Galerkin ROM(▪▪▪), stabilized ROMs using $\varepsilon' = 0$ (——) and stabilized ROMs using $\varepsilon' = \varepsilon'_{stab}$ (——). 59

7.6 PSD of the turbulent kinetic energy of the lid driven cavity as predicted by the DNS (▬) and stabilized ROMs using $\varepsilon' = \varepsilon'_{stab}$ of order $n = 5$ (——), 10 (——) and 20 (——). 60

7.7 Kinetic energy balance of stabilized ROMs of the lid driven cavity. . . 60

7.8 Evolution of the turbulent kinetic energy of the mixing layer as predicted by the DNS(▬), the standard POD-Galerkin ROM(▪▪▪), stabilized ROMs using $\varepsilon' = 0$ (——) and stabilized ROMs using $\varepsilon' = \varepsilon'_{stab}$ (——). 62

7.9 PSD of the turbulent kinetic energy of the mixing layer as predicted by the DNS (▬) and stabilized ROMs using $\varepsilon' = \varepsilon'_{stab}$ of order $n = 5$ (——), 10 (——) and 20 (——). 63

7.10 Kinetic energy balance of stabilized ROMs of the mixing layer. 63

7.11 Reconstructions of the vorticity field of the lid-driven cavity at $t = 200$ using the $n = 20$, $\varepsilon' = \varepsilon_{stab}$ stabilized ROM. The top subfigure corresponds to the DNS simulation, the middle subfigure corresponds to the optimal reconstruction using the stabilized basis function, u_i' and a_i' and the bottom subfigure corresponds to the reconstruction derived from a numerical integration of the stabilized ROM. 64

7.12 Reconstructions of the vorticity field of the mixing layer at $t = 1000$ using the $n = 20$, $\varepsilon' = \varepsilon_{stab}$ stabilized ROM. The top subfigure corresponds to the DNS simulation, the middle subfigure corresponds to the optimal reconstruction using the stabilized basis function, u_i' and a_i' and the bottom subfigure corresponds to the reconstruction derived from a numerical integration of the stabilized ROM. 65

7.13 Evolution of the turbulent kinetic energy of the lid driven cavity as predicted by the DNS at $\mathrm{Re_u} = 3 \times 10^4$(▬), $\mathrm{Re_u} = 2.5 \times 10^4$(—) and $\mathrm{Re_u} = 4.0 \times 10^4$ (- - -). 67

Acknowledgements

First and foremost, I would like to thank my advisor, Professor Earl Dowell for his support, patience, and encouragement throughout my graduate studies. I feel extremely fortunate to have an advisor who gave me the freedom to explore on my own and who provided guidance when my steps faltered. I am also grateful for the excellent support from my thesis committee: Professors Laurens Howle, Brian P. Mann and Henri Gavin. A special thanks goes out to Professor Jeff Scruggs for teaching one of the most interesting courses I have taken during my career (Linear Systems and Stochastic Dynamics). I must express my sincere thanks to Professor Bernd Noack at the Institute Pprime in Poitiers, France for offering his great insight into turbulence and model reduction. I would also like to thank Professors George Karniadakis, Charbel Farhat, Tim Colonius and Clancy Rowley for inviting me to their research groups as a visiting scholar.

Countless other friends have made the past few years absolutely delightful. A special thanks to my colleagues Firas Khasawneh, Samuel Stanton and Pascaline Cette for reminding of a life outside of the lab. A very special thanks to everyone on the Duke cycling team including Gael Hagan, Rob Ferris, Matt Rinehart and Mike Niemi. I will always remember the many adventures and colorful characters (including the elephant) at the Center for Human Science. Eric Bryant, RIP. Thanks to everyone at the Carolina photography club including Yujia Song, Fernando Cardoso and Guillaume Filteau. Finally, thanks to Demet Ulker for inspiring to pursue

graduate studies in the first place.

I am grateful for the financial support I received during the course of this research from the National Research Council of Canada Graduate Student Fellowship and the Center for Human Science Research Fellowship.

1

Introduction

Numerical simulation of fluid flows is usually a very computationally intensive endeavor. Even when adequate computational resources are available, numerical simulations often provide too little understanding of the solutions they produce. There are significant scientific and engineering benefits in developing and studying Model Order Reduction (MOR) techniques capable of producing Reduced Order Models (ROMs) of complex fluid flows that retain physical fidelity while substantially reducing the size and cost of the computational model.

Many MOR techniques involve a form of coordinate transformation where the residual is constrained to be orthogonal to the space spanned by the new coordinate system. Under this projection framework, the model order reduction problem can be stated as follows: (1) find a new coordinate system that is aligned with some important characteristics of the system (kinetic energy for example) and (2) ensure the orthogonal projection preserves some important dynamical characteristics (stability for example) of the original system. For fluid flow problems the first objective is usually satisfied by the Proper Orthogonal Decomposition (POD). The POD produces a coordinate transformation that is optimal with respect to the kinetic energy

of the fluid flow. Satisfying the second objective is usually more difficult. It is well known that orthogonal projections do not in general preserve stability. A stable, full-order model may have unstable ROMs even when the coordinate transformation and projection is fully accurate [50, 39]. Rigorous methodologies for deriving stable and accurate ROMs are available, but these are only applicable to full-order systems that are linear [79]. For example, in the balanced truncation approach, stable ROMs are derived by choosing a coordinate transformation that is oriented with the most observable and controllable states of the full order system. ROMs derived using balanced truncations are guaranteed to be stable and ROM convergence is guaranteed in the H-Infinity norm. The concept of balanced truncation has been applied to linearized fluid flows and various variants of the approach including approximate balancing have been proposed [9, 2, 78, 54]. The drawback of balanced truncation are the high computational costs associated with finding the most controllable and observable states of the full-order system. When the full-order system is nonlinear, e.g. the Navier-Stokes equations, no general methodologies for preserving stability and or accuracy are available. Unstable projection-based ROM of the Navier-Stokes equations are commonly observed in practice but are not often published. This is especially true for projection-based ROMs of turbulent Navier-Stokes flows.

Turbulence is a fluid flow regime characterized by chaotic dynamics in both space and time. In the limit of high Reynolds numbers, the dynamics of turbulence are qualitatively universal: large scale flow features are broken down into smaller and smaller scales until the scales are fine enough that viscous forces can dissipate their energy [38]. The reason ROMs derived from the standard POD projection MOR approach are prone to instabilities is because POD, by construction, is biased towards the large, energy containing scales. Therefore, ROMs generated using only the first most energetic POD basis functions are not endowed with the natural energy dissipation tendency of the smaller, lower energy viscous scales. This is especially

problematic because viscous dissipation is the only form of energy dissipation in the incompressible Navier-Stokes.

Currently, two broad categories of ROM stabilization for the Navier-Stokes equations are available: (1) direct modeling of small scale dynamics of the turbulent flow by inclusion of a sufficiently large number of POD basis functions and (2) approximate modeling of small scale dynamics using empirical turbulence models. Unfortunately, both stabilization methods are often undesirable. Stabilization through inclusion of a large number of POD basis functions creates very large POD-Galerkin ROMs that are very computationally expensive to solve. Stabilization through addition of empirical eddy viscosity terms is possible but generally undesirable because the empirical terms modify the dynamics of the original Navier-Stokes equations [51, 5, 72, 64]. In this thesis a new approach to stabilization of projection based ROMs of the Navier-Stokes equations is proposed.

1.1 Contribution of the present work to Model Order Reduction (MOR)

The objective of the work summarized in this thesis has been to develop a stabilization methodology for projection-based ROMs of turbulent Navier-Stokes fluid flows. The major contributions of this work are as follows:

1. **Direct simulation of turbulent Navier-Stokes fluid flows using the standard POD-Galerkin approach** - As discussed, there are two traditional approaches to resolve dissipative scales in projection based ROMs. Directly, via inclusion of higher order spatial basis functions, and indirectly, using empirical turbulent models. Both standard approaches have significant limitations. Curiously, although literature utilizing the indirect approach (empirical turbulence modeling) abound, there is no documented successful application of the direct approach (inclusion of higher order POD basis functions). Although, heuristi-

cally, the concept of resolving dissipative flow scales by including higher order POD basis functions seems valid, we believe validating this approach answers an important research question. Therefore, we attempt to simulate a turbulent fluid flow inside a lid-driven cavity using a very high order POD-Galerkin ROM. We show that it is indeed possible to fully resolve small scale flow dynamics through the addition of POD basis functions; our highest order model utilizes 200 POD basis functions.

2. **A new non-empirical stabilization methodology**- we propose a new, non-empirical stabilization methodology for low-order, projection based ROMs of the Navier-Stokes. The proposed stabilization methodology involves deriving a set of spatial basis functions different from the standard POD basis functions. Compared to the standard POD basis functions, these new basis functions include a greater proportion of small, dissipative scales of the turbulent flow. The proposed methodology is formulated as a small-scale constrained nonlinear optimization problem.

1.2 Thesis outline

The second chapter of this thesis provides an overview of the general projection based MOR approach. Chapter 3 provides details of the two Navier-Stokes test cases used in this thesis: the lid-driven cavity and the mixing layer. In Chapter 4 details of the POD basis functions for the two test cases are presented. In Chapter 5 the standard POD-Galerkin MOR approach is used to derive ROMs of the lid-driven cavity and the mixing layer. In Chapter 6 the new non-empirical stabilization methodology is presented and the numerical algorithm is summarized. The new stabilization approach is applied to the two Navier-Stokes flows and the results are summarized in Chapter 7. Finally, in Chapter 8, summaries are presented of the important

results of the thesis, the specific contributions of the thesis, and recommended future research directions.

2

Methodology

This chapter contains a summary of the general projection-based Model Order Reduction (MOR) approach.

2.1 Spectral methods

Spectral methods are a class of numerical techniques used to numerically discretize and solve certain classes of differential equations [13, 14, 15, 71, 33]. For example, consider a dynamical system that evolves in a Hilbert space H, $u(t) \in H$ governed by

$$\dot{u} = X(u) \tag{2.1}$$

where X is a vector field on H. Often, the governing variable u is spatio-temporal, $u = u(x,t)$, $x \in \Omega$, $t \in [0,T]$ and thus X is a spatial differential operator. In the spectral approach, the governing variable, $u(x,t)$ is discretized using separable basis functions, $a_i(t)$ and $u_i(x)$

$$u(x,t) \approx u^{[1,\ldots,n]} \equiv \sum_i a_i(t) u_i(x) \tag{2.2}$$

where $\{u_i \in H | \, i = 1, \ldots, n\}$ is a basis for the subspace of H. In the method of lines, the spatial basis functions u_i are known a priori and the goal, therefore, is to find temporal coefficients, a_i that satisfy the differential equation in some sense. In general, the origin and/or form of the spatial basis functions, u_i is arbitrary. In the context of spectral methods in Computational Fluid Dynamics (CFD) the spatial basis functions, u_i are usually analytical functions such as trigonometric functions and power functions, i.e. Chebyshev polynomials. The benefits of these functions are that their spatial derivatives are known analytically and that numerically efficient algorithms such as the Fast Fourier Transform (FFT) can be used to solve the spectral problem, i.e. finding temporal coefficients, a_i that satisfy the differential equation. In fluid flow applications, the spatial basis functions can be derived from a priori completeness requirements [35, 40], from Navier-Stokes-based eigenfunctions [32], or a posteriori from solution data set, like the Proper Orthogonal Decomposition (POD) [31] or the Dynamic Mode Decomposition (DMD) [56, 61].

The main benefit of the spectral discretization is the very favorable numerical convergence. It can be shown that spectral discretizations of many dynamical systems converge exponentially while more familiar numerical discretization methods, such as finite difference and finite element, converge only algebraically [13]

In the weighted residuals method, the temporal coefficients, a_i of the spectral discretized dynamical system are chosen such that the error is orthogonal to a subspace of H. Let $\{v_i \in H | \, i = 1, \ldots, n\}$ be a basis for a subspace of H. We seek a_i such that

$$\left\langle v_i, \dot{u}^{[1,\ldots,n]} \right\rangle_\Omega - \left\langle v_i, X\left(u^{[1,\ldots,n]}\right) \right\rangle_\Omega = 0 \tag{2.3}$$

where $\langle \cdot, \cdot \rangle_\Omega$ is an appropriately defined spatial inner product. Galerkin projection is a special form of weighted residuals where $v_i \equiv u_i$. The projection yields a set of evolution equations for the temporal coefficients a_i

$$\dot{a}_i = f_i(a) \tag{2.4}$$

Given a set of initial conditions the evolution equation can be integrated using standard ODE techniques.

2.2 Proper orthogonal decomposition (POD)

The Proper Orthogonal Decomposition (POD) is a very general information compression technique that is applicable to a wide variety of problems including digital image compression [53], signal processing [73] and bioinformatics [74]. POD is a method of deriving spatial and temporal basis functions that are in some ways "optimal" with respect to a data set provided. For incompressible fluid flows, the POD optimality condition can be expressed as follows

$$\begin{aligned} \underset{\boldsymbol{u},a}{\arg\min} \quad & \int_T \left\| \boldsymbol{u}_s - \boldsymbol{u}^{[1,\ldots,n]} \right\|_\Omega^2 dt \\ \text{s.t.} \quad & (1)\ \left\langle \boldsymbol{u}_i, \boldsymbol{u}_j \right\rangle_\Omega = \int_\Omega \boldsymbol{u}_i(\boldsymbol{x}) \cdot \boldsymbol{u}_j(\boldsymbol{x}) d\boldsymbol{x} = \delta_{ij} \\ & (2)\ \left\langle a_i, a_j \right\rangle_T = \frac{1}{T} \int_T a_i(t) a_j(t) dt = \lambda_i \delta_{ij} \end{aligned} \tag{2.5}$$

where, $\boldsymbol{u}_s(\boldsymbol{x}, t)$ is a snapshot of the fluid velocity field provided by a Direct Numerical Simulation (DNS), δ_{ij} is the Kronecker delta and λ_i are the POD eigenvalues. The discretized equivalent of Eq. (2.5) is solved using the well known Eckart-Young theorem [23] of Singular Value Decomposition (SVD). Let the matrices $\boldsymbol{\Psi}$, $\boldsymbol{\Theta}$ and $\mathbf{A}$ identify a discrete sampling of the functions u_s, $u_i(x)$ and $a_i(t)$ such that the i^{th} row and j^{th} column correspond to

$$\begin{aligned} \Psi_{ij} &\equiv u_s(x_i, t_j) \\ \Theta_{ij} &\equiv u_j(x_i) \\ A_{ij} &\equiv a_i(t_j) \end{aligned} \tag{2.6}$$

The minimization problem Eq. (2.5) can then be restated in discrete form in terms of the Frobenius norm

$$\begin{aligned} &\underset{\mathrm{rk}(\mathbf{\Theta}),\mathrm{rk}(\mathbf{A})=n}{\arg\min} && \left\| \mathbf{\Psi} - \mathbf{\Theta}\mathbf{A}^T \right\|_F \\ &\text{s.t.} && (1)\ \mathbf{\Theta}^T\mathbf{\Theta} = \mathbf{I} \\ & && (2)\ \mathbf{A}\mathbf{A}^T = diag\{\lambda\} \end{aligned} \tag{2.7}$$

By the Eckart-Young theorem [23], given a Singular Value Decomposition (SVD) of the solution matrix

$$\mathbf{\Psi} = \mathbf{U}\mathbf{\Sigma}\mathbf{V}^{\mathbf{T}} \tag{2.8}$$

the minimization problem, Eq. (2.7) is satisfied by setting the basis functions stored in the matrix $\mathbf{\Theta}$ equal to the first n left singular vectors of the solution matrix $\mathbf{\Psi}$

$$\mathbf{\Theta} = \mathbf{U}(:, 1:n) \tag{2.9}$$

while the temporal functions, $\mathbf{A}$ are equal to

$$\mathbf{A} = \mathbf{\Sigma}(1:n, 1:n)\mathbf{V}(:, 1:n)^T \tag{2.10}$$

For very thin snapshot matrices, it is computationally advantageous to compute the basis functions, i.e. the left singular vectors $\mathbf{U}$, in two steps [66]. In the first step, the right singular vectors, $\mathbf{V}$ and singular values, $\mathbf{\Sigma}$ are determined from an eigenvalue decomposition of the correlation matrix

$$\mathbf{\Psi}^T\mathbf{\Psi} = \mathbf{V}\mathbf{\Sigma}^2\mathbf{V}^T \tag{2.11}$$

Note that Eq. (2.11) is simply Eq. (2.8) left multiplied by $\mathbf{\Psi}^T$ with the observation that $\mathbf{\Psi}^T\mathbf{U} = \mathbf{V}\mathbf{\Sigma}$. In the second step, the left singular vectors $\mathbf{U}$, are found using

$$\mathbf{U} = \mathbf{\Psi}\mathbf{V}\mathbf{\Sigma}^{-1} \tag{2.12}$$

Note that Eq. (2.12) is simply Eq. (2.8) right multiplied by $\mathbf{V}\mathbf{\Sigma}^{-1}$ with the observation that $\mathbf{V}\mathbf{V}^T = \mathbf{I}$. The drawback of this two step approach is that forming the product $\mathbf{\Psi}^T\mathbf{\Psi}$ roughly squares the condition number, so the eigenvalue solution is likely less accurate. Fortunately, for many practical applications this has not proved to be a major issue.

2.3 Projection-based ROMs of the Navier-Stokes equation

The evolution of velocity field, $\boldsymbol{u}(\boldsymbol{x}, t)$ of an incompressible Newtonian fluid is governed by the Navier-Stokes equations

$$\nabla \cdot \boldsymbol{u} = 0 \tag{2.13a}$$

$$\frac{\partial \boldsymbol{u}}{\partial t} = \nu \Delta \boldsymbol{u} - \nabla \cdot (\boldsymbol{u}\boldsymbol{u}) - \nabla p \tag{2.13b}$$

The standard projection-based MOR approach to these equations utilizes a Galerkin projection of POD spatial basis functions [41, 20, 18, 31, 43, 50, 55, 67, 69, 65, 64, 1]. In the standard approach, the fluid the velocity vector, $\boldsymbol{u}(\boldsymbol{x}, t)$ is discretized spectrally using separable spatial, $\boldsymbol{u}_i(\boldsymbol{x})$ and temporal, $a_i(t)$ basis functions

$$\boldsymbol{u}(\boldsymbol{x}, t) \approx \boldsymbol{u}^{[0,\cdots,n]} = \boldsymbol{u}_0 + \sum_{i=1}^{n} a_i(t)\boldsymbol{u}_i(\boldsymbol{x}) \tag{2.14}$$

where $\boldsymbol{u}_0$ is the temporal mean. Reduced Order Models (ROM) of the Navier-Stokes are obtained via a orthogonal, i.e Galerkin projection of the residual of the Navier-Stokes onto the space spanned by spatial basis functions, $\boldsymbol{u}_i(\boldsymbol{x})$. Projection yields a set of n coupled and nonlinear Ordinary Differential Equations (ODEs) in the following canonical form

$$\dot{a}_i = \sum_{jk}^{n} Q_{ijk} a_j a_k + \sum_{j}^{n} D_{ij} a_j + b_i \qquad i = 1, \cdots, n \tag{2.15}$$

For divergence-free spatial basis functions and steady dirichlet boundary conditions, the Galerkin matrices are of the form

$$Q_{ijk} = \langle \boldsymbol{u}_i, \nabla \cdot (\boldsymbol{u}_j \boldsymbol{u}_k) \rangle_\Omega \tag{2.16a}$$

$$D_{ij} = \langle \boldsymbol{u}_i, \nu \Delta \boldsymbol{u}_j - \nabla \cdot (\boldsymbol{u}_0 \boldsymbol{u}_j) - \nabla \cdot (\boldsymbol{u}_j \boldsymbol{u}_0) \rangle_\Omega \tag{2.16b}$$

$$b_i = \langle \boldsymbol{u}_i, \nu \Delta \boldsymbol{u}_0 - \nabla \cdot (\boldsymbol{u}_0 \boldsymbol{u}_0) \rangle_\Omega \tag{2.16c}$$

For open flows the pressure term cannot be ignored but in practice is rarely modeled in full. For example, the contribution from the pressure term can usually be modeled well using a linear fit of the linear Galerkin terms, D_{ij} [26, 42]. It is important to note that the instabilities commonly encountered in POD-Galerkin ROMs of the Navier-Stokes are not a result of these pressure term approximations. Similar instabilities are known to characterize ROMs derived from the vorticity formulations of the Navier-Stokes [20].

In the context of MOR, Eq. (2.15) is a ROM of the Navier-Stokes equations with respect to the n spatial basis functions chosen in Eq. (7.3). Given initial conditions $\boldsymbol{a}(t_0) = \boldsymbol{a}_0$ the ROM can be integrated in time numerically and the full flow field can be reconstructed via Eq. (7.3).

2.4 ROM accuracy and stability

Accuracy and stability are quantified by the turbulent kinetic energy, $E(t)$ defined as

$$E(t) \equiv \frac{1}{2} \int_\Omega |\boldsymbol{u}(\boldsymbol{x}, t)|^2 \, dx \tag{2.17}$$

In the projection-based MOR approach, the flow-field, $\boldsymbol{u}(\boldsymbol{x}, t)$ is discretized spectrally as in Eq. (7.3). When the spatial basis functions used in the spectral discretization are orthonormal, the turbulent kinetic energy can be expressed as a function of the

temporal basis functions only

$$E(t) = \frac{1}{2}\sum_{i=1}^{n} a_i(t)^2 \tag{2.18}$$

When calculating the turbulent kinetic energy, $E(t)$ using Eq. (2.18) a distinction must be made with regards to what temporal basis functions, a_i are used. By the Eckart-Young theorem [23], the temporal and spatial basis functions derived via a POD decomposition of the snapshot matrix provide the optimal reconstruction of $E(t)$. Due to truncation and discretization errors, the temporal coefficients derived using a numerical integration of the ROM are not identical to the POD temporal functions. To avoid confusion, we label the turbulent kinetic energy calculated using the POD temporal basis functions as $E_{OPT}(t)$ and the turbulent kinetic energy calculated using a numerical integration of the ROM as $E_{ROM}(t)$.

The dynamics of the Navier-Stokes equations of a turbulent flow configuration are assumed to be chaotic and the true trajectories of the temporal coefficient, a_i are assumed to lie on an attractor. A ROM is considered stable if and only if, the temporal basis functions derived from the numerical integration of the ROM are close enough to the true attractor for all time t. Distance to the attractor is quantified using the time-averaged turbulent kinetic energy, $\langle E(t)\rangle_T$. The time-average of the optimal turbulent kinetic energy is, by definition of the POD optimality condition, equal to

$$\langle E(t)\rangle_T = \frac{1}{2}\sum_{i=1}^{n} \lambda_i \tag{2.19}$$

Thus, a ROM is considered stable if and only if

$$\left| \langle E_{ROM}(t)\rangle_T - \frac{1}{2}\sum_{i=1}^{n} \lambda_i \right| \leqslant \delta_E \tag{2.20}$$

where δ_E is a precision criterion for stability.

Unlike stability, a representative definition of ROM accuracy for chaotic nonlinear systems is still a matter of debate [20]. In this paper, ROM accuracy is measured qualitatively using the statistics of the turbulent kinetic energy. A ROM is considered accurate if and only if the statistics of the predicted turbulent kinetic energy are close to statistics of turbulent kinetic energy of the optimal reconstruction.

The optimal kinetic energy reconstruction using POD basis functions is guaranteed to match the DNS in the limit of infinite n, i.e. $\lim_{n\to\infty} \langle E_{OPT}(t)\rangle_T = \langle E_{DNS}(t)\rangle$. Numerous applications of the standard POD-Galerkin MOR approach suggest that this limit is also true for the ROMs, i.e. $\lim_{n\to\infty} \langle E_{ROM}(t)\rangle_T = \langle E_{OPT}(t)\rangle$. Rigorous performance bounds for finite-order Galerkin-based ROMs of the Navier-Stokes equations are not available however, because Galerkin projection does not guarantees stability or accuracy for finite-order n projections[1]. In practice, finite-order projection-based ROMs of the Navier-Stokes equations are almost always unstable and must be stabilized artificially using empirical turbulence models. Achieving stability directly, i.e. by increasing the order of the ROM n, is not practical because the convective nonlinearities of Navier-Stokes equations render higher-order projection-based ROMs computationally very prohibitive. For example, for the incompressible Navier-Stokes equations, the computational costs scale as n^{D+2}, where D is the spatial dimension of the system. Over the years many sophisticated turbulence models have been developed [64, 11, 44, 46, 45, 18, 75, 65, 21, 49]. The drawback of empirical turbulence models is that these models, by construction, modify the dynamics of the Navier-Stokes equations and thus degrade ROM reliability and accuracy.

[1] This is true for MOR of both linear and nonlinear systems and is not alleviated by the use of "optimal" basis functions such as those derived from POD

3

Applications

This chapter describes the two prototypical Navier-Stokes flows that are used to validate the proposed methodology. Specifically, the incompressible flow inside a two-dimensional lid-driven cavity and a two-dimensional mixing layer are considered. Details of the flow parameters and boundary conditions are summarized including details of the numerical solvers. The lid-driven cavity is discussed in Section 3.1 and the mixing layer is discussed in Section 3.2.

3.1 Lid-driven cavity

The lid-driven cavity is a well known prototypical example problem used to validate fluid flow numerical schemes and reduced order models [18, 62, 70]. Specifically, isothermal, incompressible, two-dimensional flow inside a square cavity driven by a prescribed lid velocity, $\boldsymbol{u}_{lid} = (1 - x^2)^2$ is considered. Details of the boundary conditions are illustrated in Fig. 3.1 The Reynolds number (Re) is defined with respect to the maximum velocity of the lid and the width of the cavity. The Navier-Stokes are discretized in space using Chebyshev polynomials. The convective nonlinearities are handled pseudo-spectrally and the Chebyshev coefficients are derived using the

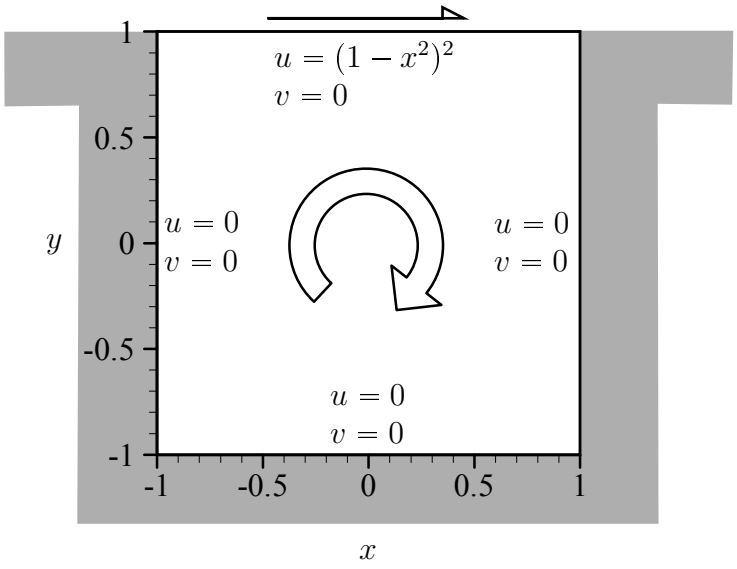

FIGURE 3.1: Boundary conditions for the lid-driven cavity test case.

Fast Fourier Transform (FFT). The Navier-Stokes are discretized in time using a semi-implicit, second-order Euler scheme. Figure 3.2 is a snapshot of a statistically stationary solution at $\mathrm{Re_u} = 3 \times 10^4$. This particular simulation was performed using a 256^2 Chebyshev grid. The computations were performed on a cluster at Duke University using 8 processors. The computational domain comprises of a 256^2 Chebyshev grid: 256 points in both the x and y directions. The simulation is first initialized over 100 000 time steps ($\Delta t = 1 \times 10^{-3}$s) which corresponds to a total run time of 8 hours. The data base is then generated: 50 000 iterations are done on 4 hours to create 5000 snapshots, sampled at $f_s = 10$ Hz. The turbulent kinetic energy, $E(t)$ of the lid-driven cavity as predicted by the Direct Numerical Simulation (DNS) of the Navier-Stokes equations is illustrated in Fig. 3.3. The time-average of the turbulent kinetic-energy predicted by the DNS is $\langle E_{DNS}(t) \rangle_T = 9.347 \times 10^{-4}$.

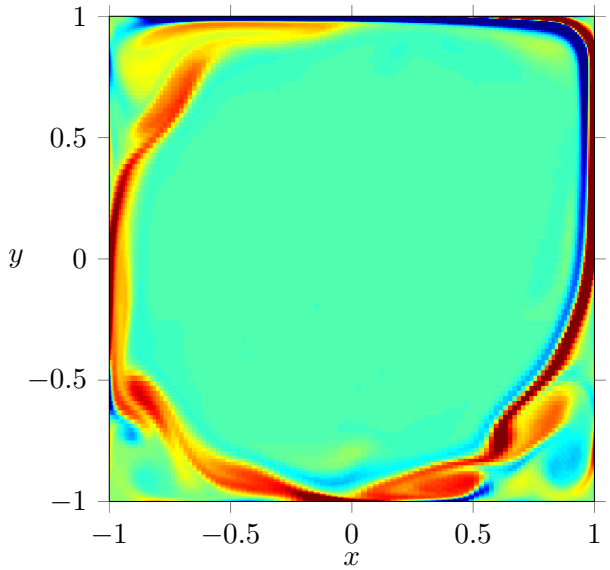

FIGURE 3.2: Vorticity contours from a DNS of the lid-driven cavity at $\mathrm{Re_u} = 3 \times 10^4$

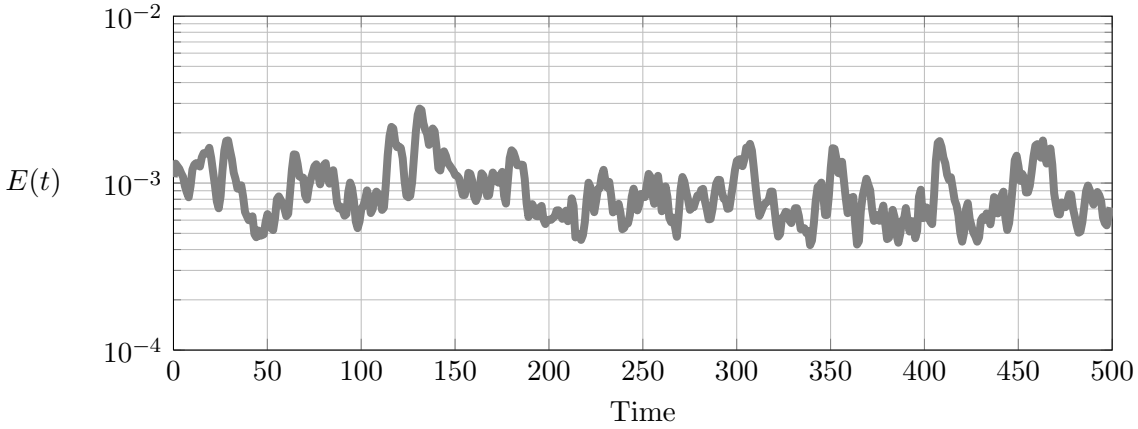

FIGURE 3.3: Evolution of the turbulent kinetic energy of the lid-driven cavity as predicted by the DNS: $E_{DNS}(t)$(▬).

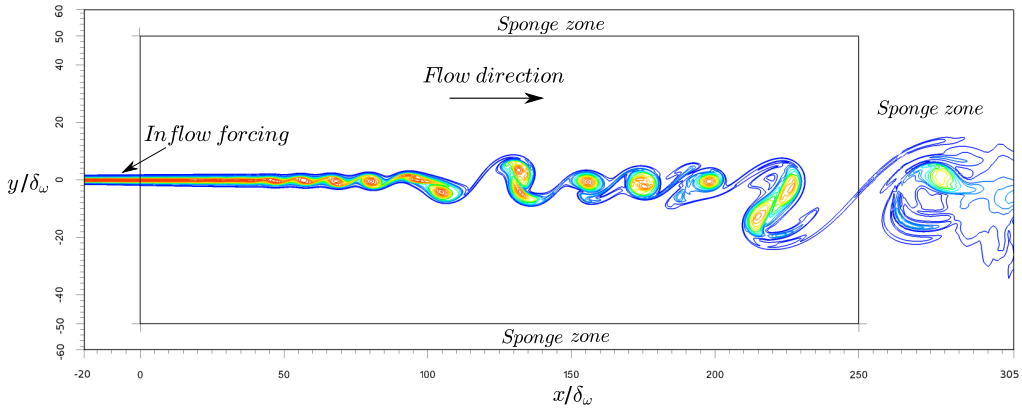

FIGURE 3.4: Boundary conditions for mixing layer test case.

3.2 Mixing layer

The data base used for the present work corresponds to the DNS of a compressible isothermal 2-D mixing layer. Details of the boundary conditions are illustrated in Fig. 3.4 The numerical algorithm is the same as that employed previously for studies on jet noise sources [17]. The full Navier-Stokes equations for 2-D fluid motion are formulated in Cartesian coordinates and solved in conservative form. Spatial derivatives are computed with a fourth-order-accurate finite scheme for both the inviscid and viscous portion of the flux [30, 27]. A second-order predictor-corrector scheme is used to advance the solution in time. In addition, block decomposition and MPI parallelization are implemented. The three-dimensional Navier-Stokes characteristic non-reflective boundary conditions (3D-NSCBC), developped in [37], are applied at the boundaries of the computational domain to account for convective fluxes and pressure gradients across the boundary plane. In order to simulate anechoic boundary conditions, the mesh is stretched and a dissipative term is added to the equations, in the sponge zone [19]. A detailed description of the numerical procedure is given in [22].

The inflow mean streamwise velocity profile is given by a hyperbolic tangent

profile

$$\overline{u}(y) = U_2 + \frac{1}{2}\Delta U\left[1 + \tanh(2y)\right] \tag{3.1}$$

with $\Delta U = U_1 - U_2$ the velocity difference across the mixing layer, where U_1 and U_2 are the initial velocity above and below, respectively. The velocities, lengths, and time are nondimensionalized with ΔU and the initial vorticity thickness δ_ω. The flow Reynolds number is $Re = \delta_\omega \Delta U/\nu_a = 500$ where the subscript $(\cdot)_a$ indicates a constant ambient quantity. The Mach number of the free streams are $M_1 = U_1/c_a = 0.1$ and $M_2 = U_2/c_a = 0.033$, where c_a is the sound speed. The inflow mean temperature is calculated with the Crocco-Busemann relation, and the inflow mean pressure is constant. The Prandtl number is selected to be $Pr = 0.7$. Finally, the convective Mach number is given by $M_c = \Delta U/2c_a = 0.033$, so that the flow can be assumed as quasi-incompressible. The numerical code was extensively validated against numerical and experimental data; some results can be found in [17, 22]. The computations were performed on the cluster of the PPRIME Institute in Poitiers, France using 64 processors. The computational domain comprises approximately 2.1 million grid points: 2367 points in the streamwise direction, and 884 points along the y direction. The extension of the computational domain is $325\delta_\omega \times 120\delta_\omega$. The sponge regions are from $x = -20\delta_\omega$ to $x = 0$ and $x = 250\delta_\omega$ to $x = 305\delta_\omega$ in the streamwise direction, and from $\pm 50\delta_\omega$ to $\pm 60\delta_\omega$ in the transverse y direction. In the shear layer ($-10 \leqslant y/\delta_\omega \leqslant 10$), the grid spacing in the y direction is uniform. This value $\Delta y_{\min} = 0.07\delta_\omega$ corresponds to the minimum grid spacing in the y direction. The grid is then stretched using error functions as in [76]. The parameters of the stretching are chosen to give a maximum spacing $\Delta y_{\max} = 0.9\delta_\omega$ at $y = \pm 60\delta_\omega$. In the physical domain ($0 \leqslant x/\delta_\omega \leqslant 250$), the grid spacing in the x direction is uniform and equal to $\Delta x_{\min} = 1.7\Delta_0$. In the sponge regions, similar mapping functions are used along x, to match $\Delta x_{\max} = 0.9\delta_\omega$ at $x = -20\delta_\omega$ and $\Delta x_{\max} = 2\delta_\omega$ at $x = 305\delta_\omega$.

To promote a natural transition to turbulence from an initially laminar solution, the flow is forced by adding at every iteration solenoidal perturbations defined as [12]

$$\begin{aligned} u(x,y,t) &= u(x,y,t) + \alpha\epsilon(t)U_c\frac{(y-y_0)}{\Delta y_{\min}}\,\exp\left\{-\ln(2)\frac{(x-x_0)^2+(y-y_0)^2}{\Delta y_{\min}^2}\right\} \\ v(x,y,t) &= v(x,y,t) - \alpha\epsilon(t)U_c\frac{(x-x_0)}{\Delta y_{\min}}\,\exp\left\{-\ln(2)\frac{(x-x_0)^2+(y-y_0)^2}{\Delta y_{\min}^2}\right\} \end{aligned} \tag{3.2}$$

where $-1 \leqslant \epsilon \leqslant 1$ is a random number. The simulation parameters are $x_0 = -5\delta_\omega$ and $y_0 = 0$ for the location of the excitation, and $\alpha = 0.01$ for the forcing coefficient. The simulation is first initialized over 330 000 time steps ($\Delta t = 1.8 \times 10^{-8}$s) which corresponds to a total run time of 35 hours. The data base is then generated: 1 093 695 iterations are done on 115 hours to create 2000 snapshots, sampled at $f_s = 100$ kHz. The turbulent kinetic energy, $E(t)$ of the mixing layer as predicted by

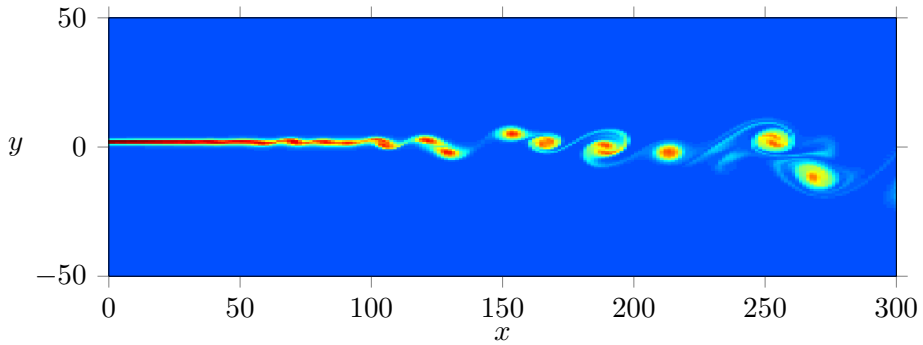

FIGURE 3.5: Vorticity contours from a DNS of the mixing at $\mathrm{Re}_{\delta_\omega} = 500$

the DNS is illustrated in Fig. 3.6. The time-average of the turbulent kinetic-energy predicted by the DNS is $\langle E_{DNS}(t)\rangle_T = 75.55$.

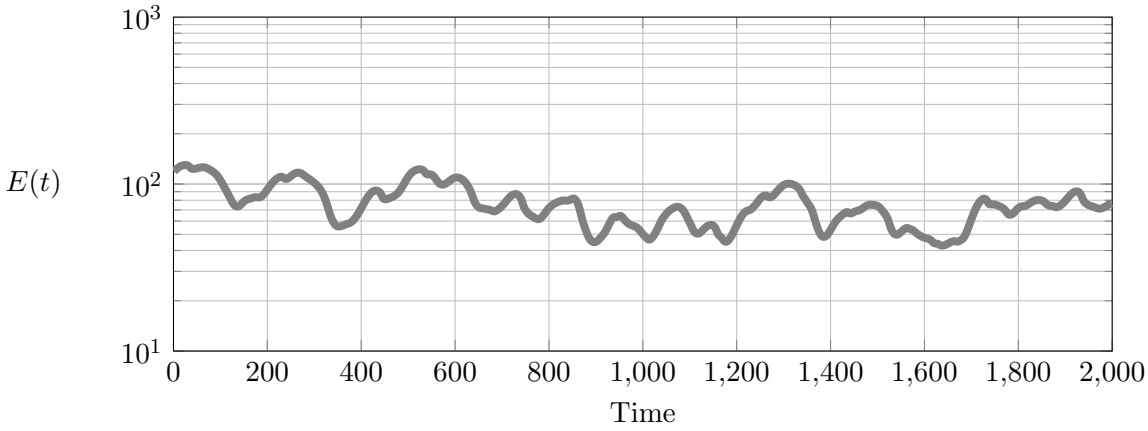

FIGURE 3.6: Evolution of the turbulent kinetic energy of the mixing layer as predicted by the DNS: $E_{DNS}(t)$(▬).

4

Proper Orthogonal Decomposition

This chapter summarizes the results of a POD of the lid-driven cavity and the mixing layer. A select number of spatial and temporal POD basis functions are illustrated and the percentage of overall kinetic energy captured is summarized. In Section 4.3 the evolution of the turbulent kinetic energy of the two test cases is reconstructed using the POD basis functions.

4.1 POD basis functions of the lid-driven cavity

A database of 5000 DNS snapshots of the lid-driven cavity were used to find POD spatial, $\boldsymbol{u}_i(\boldsymbol{x})$ and POD temporal, $a_i(t)$ basis functions. The nondimensional time interval between each snapshot equaled 0.1. Increasing the number of snapshots or the time interval between each snapshot had no significant effect on the performance characteristics of the ROMs. The MATLAB code used to compute the basis functions is presented in Appendix A.1. The percentaged of time-averaged, turbulent kinetic energy captured by the i^{th} POD basis functions is labeled, $\tilde{E}_i$ and defined as follows

$$\tilde{E}_i = \frac{\lambda_i}{\sum_{i=1}^{N} \lambda_i} \times 100 \tag{4.1}$$

where N is a large number of basis functions that adequately approximates the DNS. For the lid-driven cavity a total of 500 POD basis functions were identified and so a total of $N = 500$ eigenvalues are used to approximate the time-averaged, turbulent kinetic energy of the DNS. Results for the lid-driven cavity are shown in Table 4.1. Figure 4.1 illustrates the vorticity contours of the mean mode, $\boldsymbol{u}_0(\boldsymbol{x})$ of the lid-driven

i	$\tilde{E}_i$
1	16.12
2	13.21
3	8.275
4	7.459
5	5.300
⋮	⋮
249	4.017×10^{-3}
250	3.951×10^{-3}

Table 4.1: Percent of time-averaged, turbulent kinetic energy captured by the first 250 POD basis functions of the lid-driven cavity at $\mathrm{Re_u} = 3 \times 10^4$.

cavity at $\mathrm{Re_u} = 3 \times 10^4$. Vorticity contours of spatial POD basis functions, $\boldsymbol{u}_i(\boldsymbol{x})$

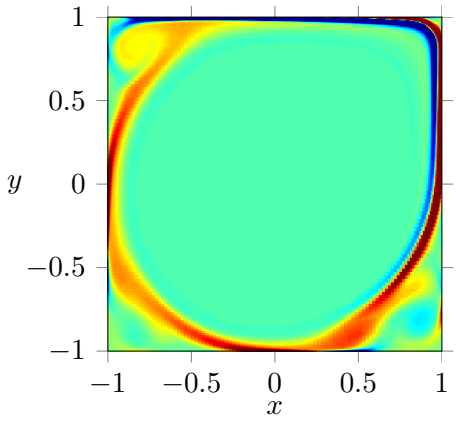

FIGURE 4.1: Vorticity contours of the mean mode, $\boldsymbol{u}_0(\boldsymbol{x})$ of the lid-driven cavity at $\mathrm{Re_u} = 3 \times 10^4$.

for $i = 1, 2, 20, 50$ and 250 of the lid-driven cavity are illustrated in Fig. 4.2. As expected, the overall spatial wave-lengths of the POD basis functions tends to increases

with order. The low-order POD basis functions correspond to the large, high-energy physical scales of the turbulent flows while the higher-order POD basis functions correspond to the small, low-energy physical scales of the turbulent flow. The corresponding temporal POD basis functions of the lid-driven cavity are illustrated in Fig. 4.3. Similarly to the spatial basis functions, the frequency content of the temporal basis functions tends to increase with order. In addition, the mean amplitude of the temporal basis functions tends to decrease with order. Figures 4.2 and 4.3 clearly illustrate the most fundamental spatio-temporal properties of turbulent flows: large, high-energy features of a turbulent flow are associated with low temporal frequencies while small, low-energy features of a turbulent flow are associated with high frequency but low amplitude temporal dynamics.

4.2 POD basis functions of the mixing layer

A database of 2000 DNS snapshots of the mixing layer were used to find the POD spatial, $\boldsymbol{u}_i(\boldsymbol{x})$ and POD temporal, $a_i(t)$ basis functions. The nondimensional time interval between each snapshot equaled 1. Increasing the number of snapshots or the time interval between each snapshot had no significant effect on the performance characteristics of the ROMs. The MATLAB code used to compute the basis functions is presented in Appendix A.1. The percentaged of time-averaged, turbulent kinetic energy captured by the POD basis functions are shown in Table 4.2. Figure 4.4 illustrates the vorticity contours of the mean mode, $\boldsymbol{u}_0(\boldsymbol{x})$ of the mixing layer at $\mathrm{Re_u} = 3 \times 10^4$. Vorticity contours of spatial POD basis functions, $\boldsymbol{u}_i(\boldsymbol{x})$ for $i = 1, 2, 20, 50$ and 150 of the mixing layer are illustrated in Fig. 4.5. Similarly to the lid-driven cavity, the overall spatial wave-lengths of the mixing layer POD basis functions tends to increases with the order, n. The low-order POD basis functions correspond to the large, high-energy physical scales of the turbulent flows while the higher-order POD basis functions correspond to the small, low-energy physical

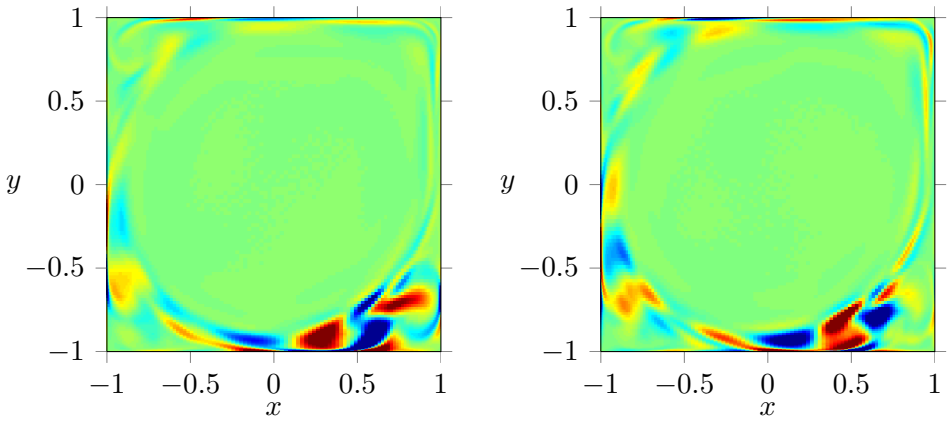

(a) $\boldsymbol{u}_1$ (b) $\boldsymbol{u}_2$

(c) $\boldsymbol{u}_{10}$ (d) $\boldsymbol{u}_{20}$

(e) $\boldsymbol{u}_{50}$ (f) $\boldsymbol{u}_{250}$

FIGURE 4.2: Vorticity contours of spatial POD basis functions of the lid-driven cavity at $\mathrm{Re_u} = 3 \times 10^4$.

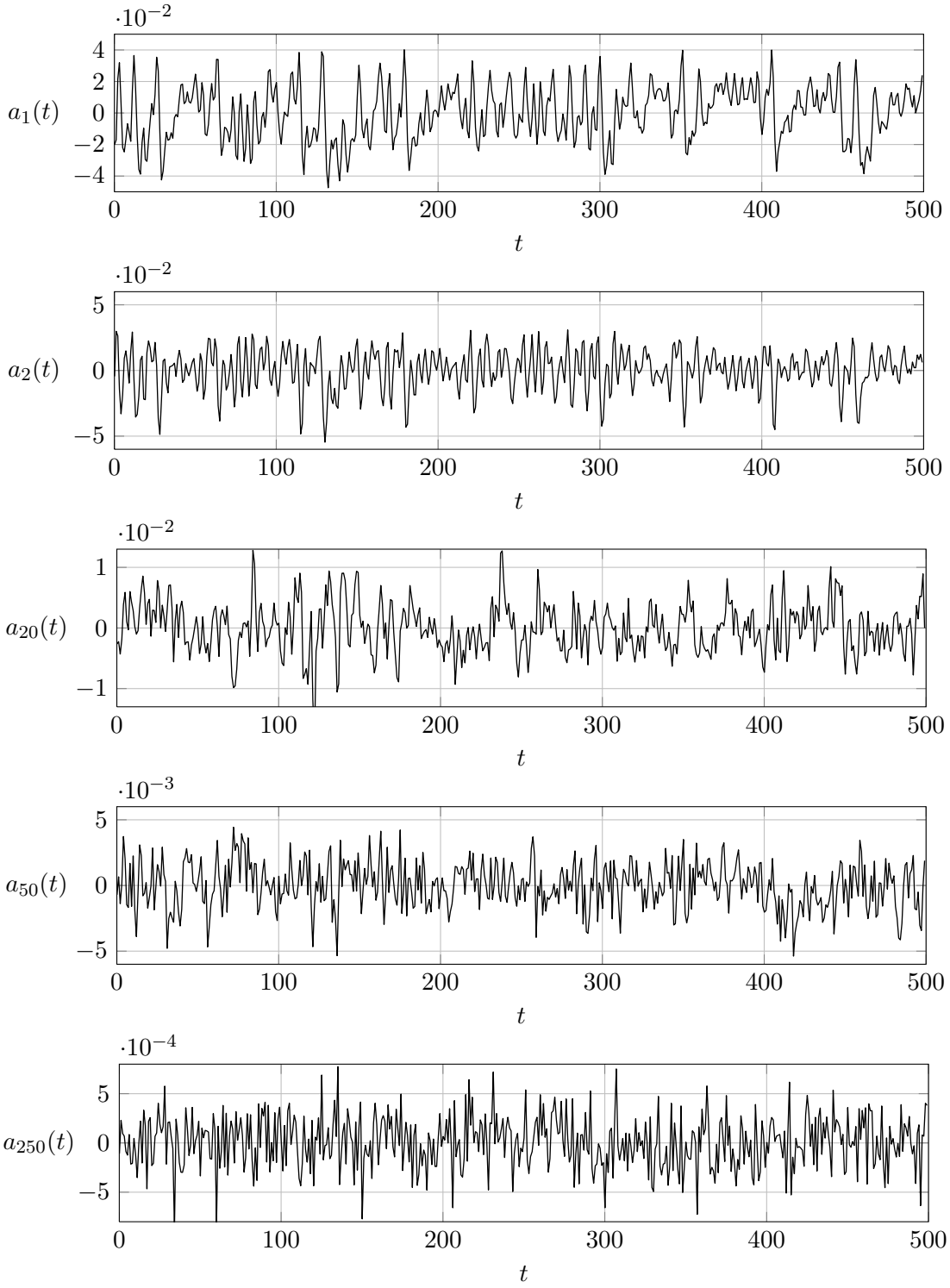

FIGURE 4.3: Evolution of the temporal POD basis functions of the lid-driven cavity at $\mathrm{Re_u} = 3 \times 10^4$.

i	$\tilde{E}_i$
1	18.35
2	16.92
3	5.594
4	5.512
5	4.335
⋮	⋮
149	1.987×10^{-3}
150	1.933×10^{-3}

Table 4.2: Percent of turbulent kinetic energy captured by the first 150 POD basis functions of the mixing layer at $\mathrm{Re}_{\delta_\omega} = 500$.

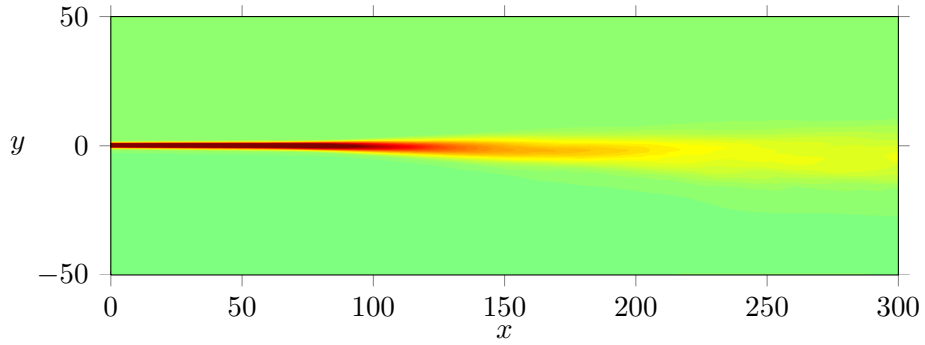

FIGURE 4.4: Vorticity contours of the mean mode, $\boldsymbol{u}_0(\boldsymbol{x})$ of the mixing layer at $\mathrm{Re}_{\delta_\omega} = 500$.

scales of the turbulent flow. The corresponding temporal POD basis functions of the mixing layer are illustrated in Fig. 4.6. Similarly to the spatial basis functions, the frequency content of the temporal basis functions tends to increase with order. In addition, the mean amplitude of the temporal basis functions tends to decrease with order. Figures 4.5 and 4.6 again illustrate a fundamental property of turbulent flows: large, high-energy features of a turbulent flow are associated with low temporal frequencies while small, low-energy features of a turbulent flow are associated with high frequency but low amplitude temporal dynamics.

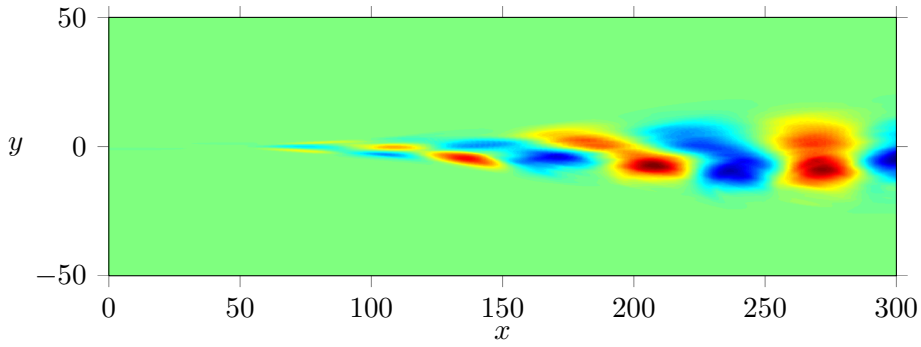

(a) $\boldsymbol{u}_1$

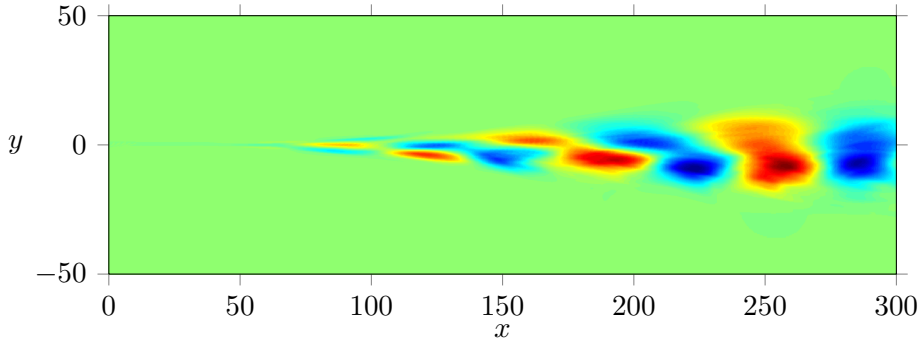

(b) $\boldsymbol{u}_2$

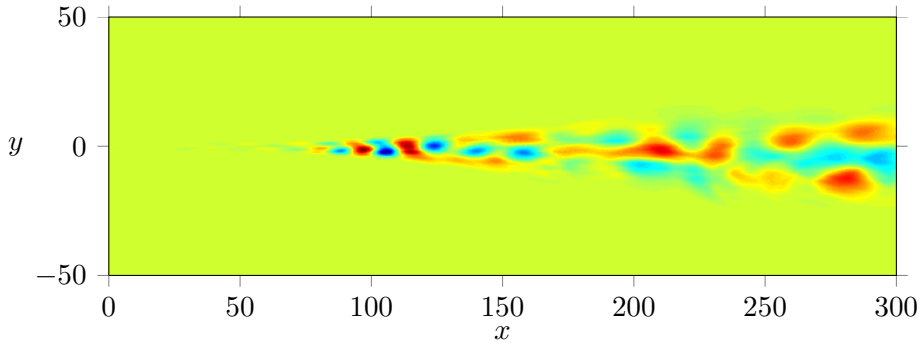

(c) $\boldsymbol{u}_{20}$

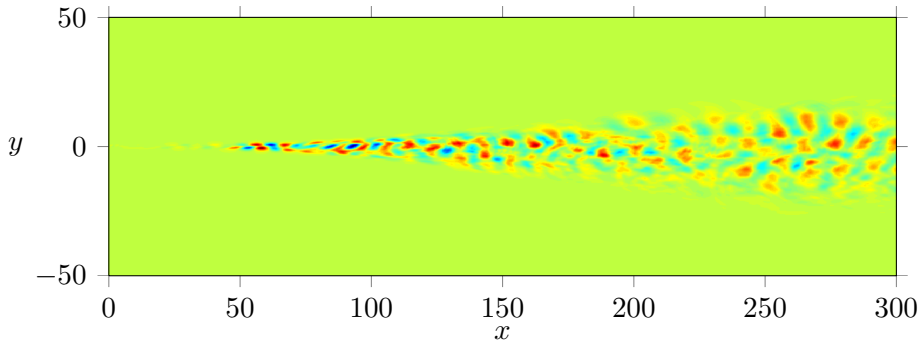

(d) $\boldsymbol{u}_{150}$

FIGURE 4.5: Vorticity contours of spatial POD basis functions of the mixing layer at $\mathrm{Re}_{\delta_\omega} = 500$.

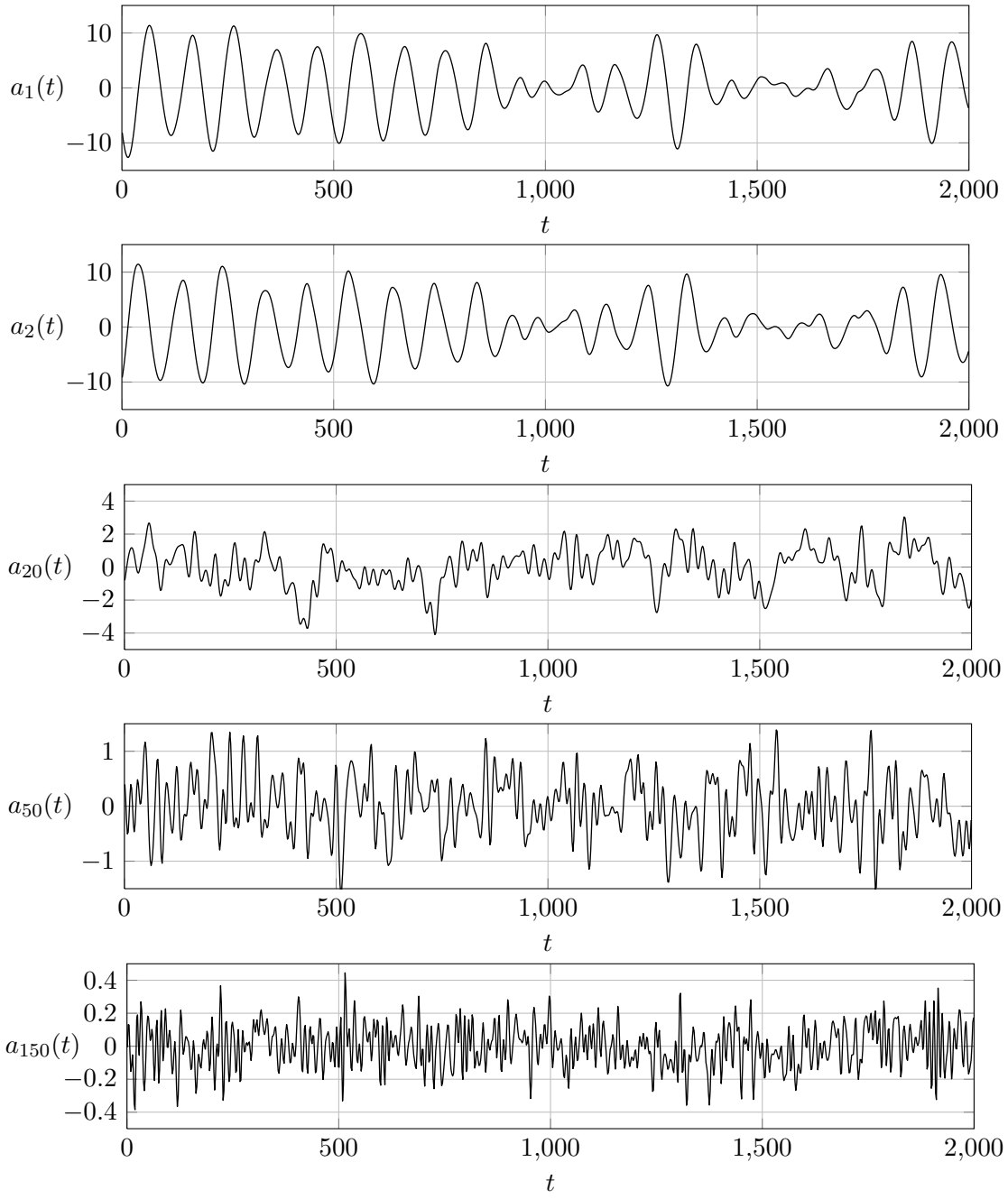

FIGURE 4.6: Evolution of the temporal POD basis functions of the mixing layer at $\mathrm{Re}_{\delta_\omega} = 500$.

4.3 Reconstruction turbulent kinetic energy, $E(t)$

In this section the turbulent kinetic energy, $E(t)$ of the lid-driven cavity and mixing layer is reconstructed using the POD basis functions. Figures 4.7 and Figures 4.8 illustrates the evolution of $E(t)$ for the lid-driven cavity and the mixing layer respectively, as predicted by the DNS and POD reconstructions of order $n = 10, 20$ and 50. For both test cases, the reconstruction of $E(t)$ using $n = 50$ POD basis functions is indistinguishable from the DNS. The time-averaged, turbulent kinetic energy, captured by the first $n = 10, 20$ and 50 POD basis functions of the lid-driven cavity are 67.16%, 82.40% and 93.60% of the DNS respectively. The time-averaged, turbulent kinetic energy, captured by the first $n = 10, 20$ and 50 POD basis functions of the mixing layer are 66.80%, 81.77% and 95.50% of the DNS respectively. The POD basis functions are optimal in that no other set of temporal and spatial basis functions will reconstruct more of the turbulent kinetic energy on the average.

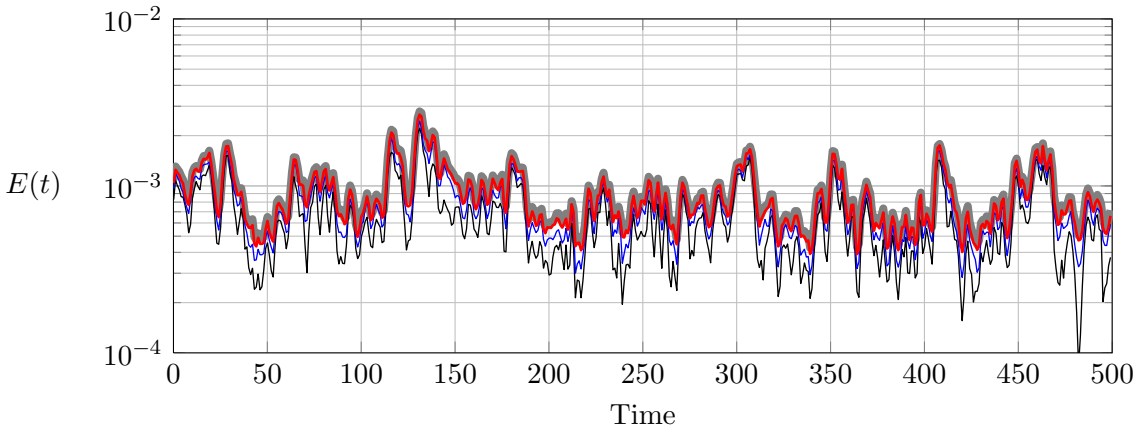

FIGURE 4.7: Reconstruction of the turbulent kinetic energy of the lid-driven cavity at $\mathrm{Re_u} = 3 \times 10^4$ using the first n POD basis functions: $n = 10$(——), $n = 20$(——) and $n = 50$(——) and compared to the DNS(——).

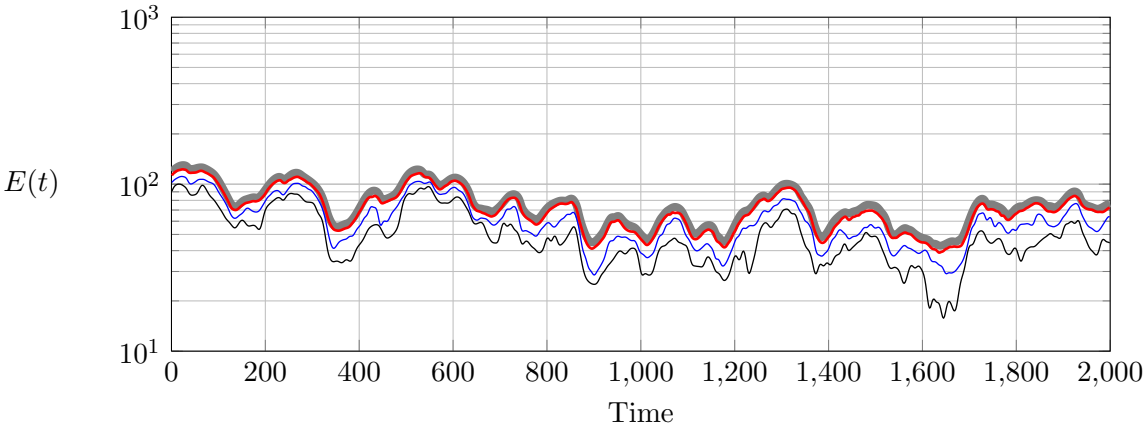

FIGURE 4.8: Reconstruction of the turbulent kinetic energy of the mixing layer at $\mathrm{Re}_{\delta_\omega} = 500$ using the first n POD basis functions: $n = 10$(——), $n = 20$(——) and $n = 50$(——) and compared to the DNS(——).

4.4 Reconstruction of the full flow field, $\boldsymbol{u}(\boldsymbol{x}, t)$

In this section the full flow field of the lid-driven cavity and mixing layer is reconstructed. The full flow field is reconstructed using the standard spectral dicretization

$$\boldsymbol{u}(\boldsymbol{x}, t) \approx \boldsymbol{u}^{[0,\cdots,n]} = \boldsymbol{u}_0 + \sum_{i=1}^{n} a_i(t)\boldsymbol{u}_i(\boldsymbol{x}) \tag{4.2}$$

where $\boldsymbol{u}_0$ is the temporal mean. Figure 4.9 illustrates the vorticity contours of the lid-driven cavity as predicted by the DNS, the optimal reconstruction using the first $n = 10$ and first 50 POD basis functions. Figure 4.10 illustrates the vorticity contours of the mixing as predicted by the DNS, the optimal reconstruction using the first $n = 10$ and first 50 POD basis functions. For both text cases, the reconstruction of the vorticity field using $n = 50$ POD basis functions is qualitatively very similar to the DNS.

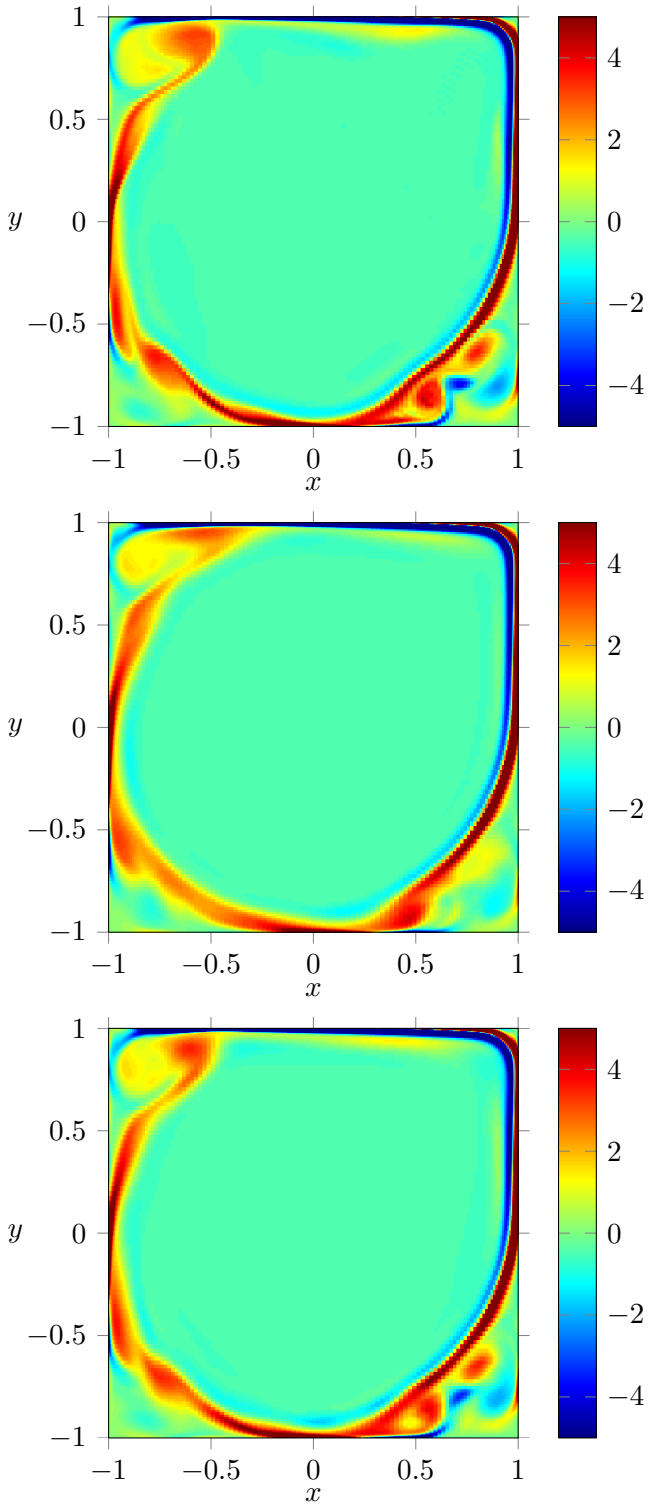

FIGURE 4.9: Reconstructions of the vorticity field of the lid-driven cavity at $t = 200$ using the first $n = 10$ and 50 POD basis functions.

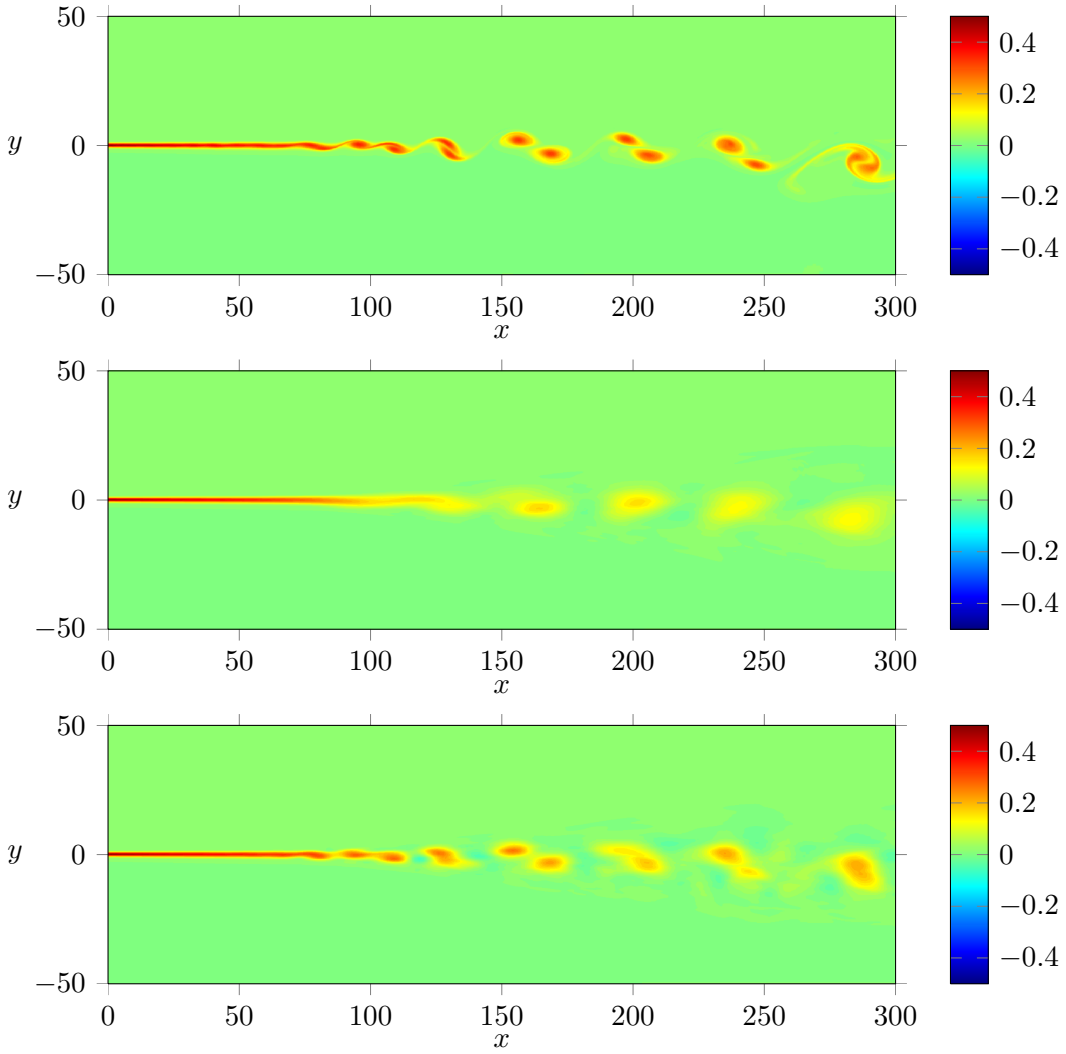

FIGURE 4.10: Reconstructions of the vorticity field of the mixing layer at $t = 1000$ using the first $n = 10$ and 50 POD basis functions.

5

The standard POD-Galerkin MOR approach

This chapter summarizes the performance characteristics of ROMs derived using the standard POD-Galerkin MOR approach for the two prototypical Navier-Stokes flows described in the preceding chapter. In Section 5.1, the incompressible flow inside a two-dimensional lid-driven cavity is modeled and in Section 5.2 the two-dimensional mixing layer is modeled. Results presented in this chapter demonstrate the strong instabilities that characterize standard POD-based ROMs of turbulent fluid flows.

5.1 Lid-driven cavity

In this section, performance characteristics of ROMs of the lid-driven cavity derived using the standard POD-Galerkin MOR approach are summarized. In the standard POD-Galerkin MOR approach, n^{th} order ROMs are derived by projecting the residual of the Navier Stokes onto the first n most energetic POD spatial basis functions, $\boldsymbol{u}_i$; details of the MATLAB code used to find the Galerkin matrices are available in Appendix A.2. The ROMs are integrated in MATLAB using the built-in adaptive forth/fifth order Runge-Kutta scheme `ODE45`. Details of the computation are available in Appendix A.3. Figure 5.1 summarizes the stability characteristics of the

standard POD-Galerkin ROMs. The turbulent kinetic energy, $E_{DNS}(t)$ as predicted by the DNS of the lid-driven cavity is identified by the thick gray curves. The optimal reconstruction of the turbulent kinetic energy given the first n POD basis functions, $E_{OPT}(t)$ is identified by the thin black curves. Finally, the turbulent kinetic energy, $E_{ROM}(t)$ as predicted by ROMs derived using the standard POD-Galerkin MOR approach is identified by the thin blue curves. The turbulent kinetic energy of the ROM is calculated using Eq. (2.18) using temporal basis functions a_i derived from the numerical integration of Eq. (2.15). Figure. 5.1 illustrates several characteristic properties of low-order ROMs derived using the standard POD-Galerkin MOR approach. First, as the number of POD basis functions is increased, the optimal kinetic energy reconstruction (thin black curves) converges to the true kinetic energy of the DNS (thick gray curves) as the number of basis functions n is increased. Second, despite the fact that the POD basis functions are capable of reconstructing the flow very accurately, i.e the black curves are very close to the thick gray curves, this accuracy is not inherited by the ROMs generated from these basis functions. In order to generate accurate and stable ROMs using the standard POD-Galerkin MOR approach significantly more POD basis functions are required. Figure 5.1 suggests that the standard POD-Galerkin MOR approach converges to the DNS as the order of the ROMs is increased. The main drawback of this approach however is that the computational costs associated with generating and simulation high-order ROMs can be prohibitive. Table 5.1 summarizes the total CPU time required to generate and simulate a ROM of order n. The CPU time includes the time required to generate the Galerkin matrices Q_{ijk}, D_{ij} and b_i and integrating the n nonlinear and coupled ODEs that define the the ROM for $t = [0, 500]$.

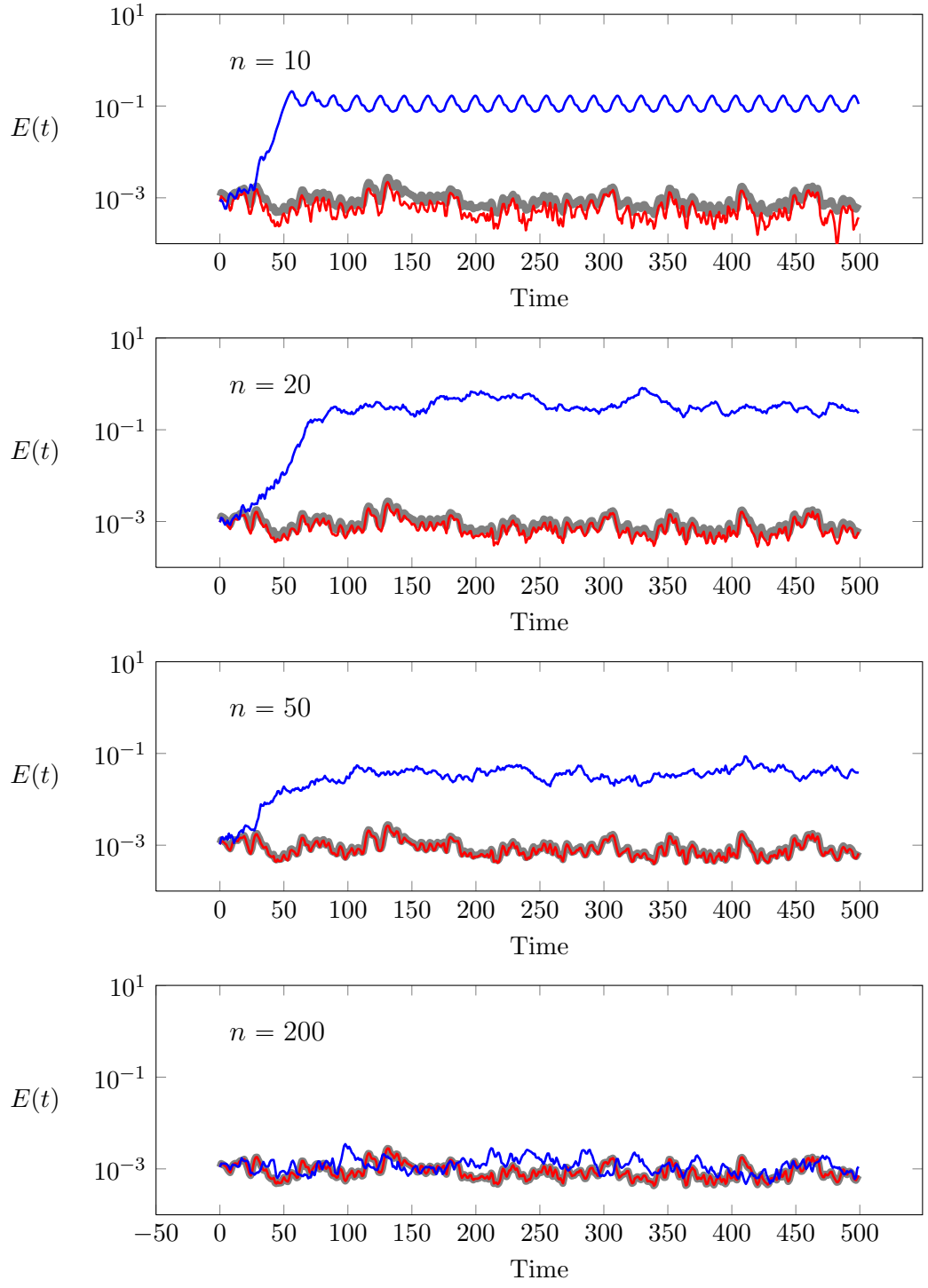

FIGURE 5.1: Evolution of the turbulent kinetic energy of the lid driven cavity as predicted by the DNS: $E_{DNS}(t)$(▬), the optimal reconstruction using the POD basis functions: $E_{OPT}(t)$(—), and the integration of a ROM derived from the standard POD-Galerkin MOR approach: $E_{ROM}(t)$(—).

n	CPU time, seconds (hours)
10	20.22
20	26.66
50	74.78
200	7452 (2.070)

Table 5.1: CPU time required to generate and integrate POD-Galerkin ROMs of the lid-driven cavity.

5.2 Mixing layer

In this section, performance characteristics of ROMs of the mixing layer derived using the standard POD-Galerkin MOR approach are summarized. Figure 5.2 summarizes the stability characteristics of the standard POD-Galerkin ROMs via the turbulent kinetic energy. The thick gray curves correspond to the turbulent kinetic energy, $E_{DNS}(t)$ as predicted by the DNS of the mixing layer. The thin black curves correspond to the optimal reconstruction of the turbulent kinetic energy, $E_{OPT}(t)$ using the first n most energetic POD basis functions. The thin blue curves correspond to the turbulent kinetic energy, $E_{ROM}(t)$ as predicted by ROMs derived using the standard POD-Galerkin MOR approach. The turbulent kinetic energy of the ROM is calculated using Eq. (2.18) using temporal basis functions a_i derived from the numerical integration of Eq. (2.15). As was the case for the lid-driven cavity, as the number of POD basis functions is increased, the optimal turbulent kinetic energy reconstruction (thin black curves) converges to the true kinetic energy of the DNS (thick gray curves) as the number of basis functions n is increased. Finally, despite the fact that the POD basis functions are capable of reconstruction the flow very accurately, i.e the black curves are very close to the thick gray curves, this accuracy is not inherited by the ROMs generated from these basis functions. Table 5.2 summarizes the total CPU time required to generate and simulate ROMs of the mixing layer. The CPU time includes the time required to generate the Galerkin matrices

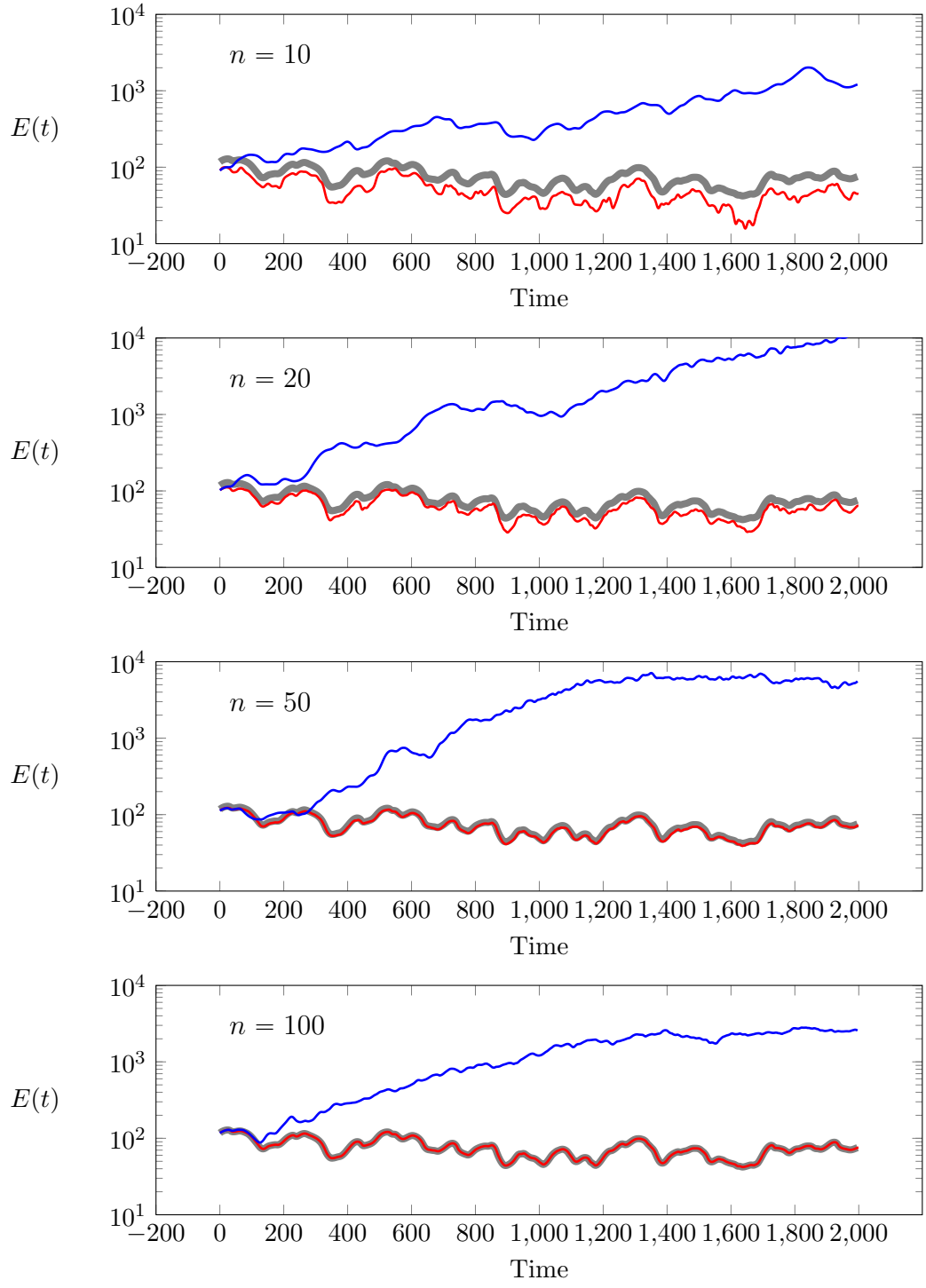

FIGURE 5.2: Evolution of the turbulent kinetic energy of the mixing layer as predicted by the DNS: $E_{DNS}(t)$(▬), the optimal reconstruction using the POD basis functions: $E_{OPT}(t)$(—), and the integration of a ROM derived from the standard POD-Galerkin MOR approach: $E_{ROM}(t)$(—).

Q_{ijk}, D_{ij} and b_i and integrating of the ROM for $t = [0, t_{\max}]$ where $t_{\max} = 2000$ in MATLAB using `ODE45`.

n	CPU time, seconds (hours)
10	38.02
20	147.9
50	2013 (0.5592)
100	64310 (17.86)

Table 5.2: CPU time required to generate and integrate POD-Galerkin ROMs of the mixing layer.

6

A new proposed stabilization approach to MOR of the Navier-Stokes equations

In this chapter a new proposed stabilization approach to projection-based ROMs of the turbulent Navier-Stokes equations is introduced. To motivate the proposed methodology, background material on common stabilization approaches for linear and nonlinear systems are first summarized.

6.1 Review of stabilization approaches for linear systems

Consider the following Linear Time Invariant (LTI) system

$$\dot{\boldsymbol{x}} = \mathbf{A}\mathbf{x} + \mathbf{B}\mathbf{u} \tag{6.1a}$$

$$\boldsymbol{y} = \mathbf{C}\mathbf{x} \tag{6.1b}$$

where $\boldsymbol{x} \in \mathbb{R}^N$ are the system sates, $\boldsymbol{u} \in \mathbb{R}^p$ are the inputs and $\boldsymbol{y} \in \mathbb{R}^q$ are the outputs. For the sake of brevity, we assume the state matrices are real, i.e $\mathbf{A} \in \mathbb{R}^{N\times N}$, $\mathbf{B} \in \mathbb{R}^{N\times q}$ and $\mathbf{C} \in \mathbb{R}^{q\times N}$ and assume the feedthrough matrix $\mathbf{D}$ is zero. In the typical projection-based MOR approach, the goal is to find coordinate transformation $\boldsymbol{x} = \boldsymbol{\Phi}\boldsymbol{x}_r$ where $\mathbf{U} \in \mathbb{R}^{N\times n}$, $\boldsymbol{x}_r \in \mathbb{R}^n$, $N > n$ and a projection $\boldsymbol{\Psi} \in \mathbb{R}^{N\times n}$ such that

the dynamics of the reduced order system

$$\dot{\hat{\boldsymbol{x}}} = \boldsymbol{\Psi}^T \mathbf{A} \boldsymbol{\Phi} \hat{\boldsymbol{x}} + \boldsymbol{\Psi}^T \mathbf{B} \boldsymbol{u} \tag{6.2a}$$

$$\boldsymbol{y} = \mathbf{C} \boldsymbol{\Phi} \hat{\mathbf{x}} \tag{6.2b}$$

approximate the dynamics of the original system in some desirable way. For example, it is usually desirable that the reduced order system is asymptotically stable, i.e. that the real components of all eigenvalues of the reduced state matrix $\hat{\mathbf{A}} = \boldsymbol{\Psi}^T \mathbf{A} \boldsymbol{\Phi}$ are less than zero $\Re\left\{\hat{\lambda}_i\right\} < 0$ for $i = 1, \cdots, n$. It can be easily demonstrated that this stability is not guaranteed for arbitrary coordinate transformations and projections[50, 55]. Consider the simple asymptotically stable homogeneous system

$$\dot{\boldsymbol{x}} = \begin{bmatrix} 1 & -1 \\ 3 & -2 \end{bmatrix} \boldsymbol{x} \tag{6.3}$$

a projection onto the first coordinate using $\boldsymbol{\Phi} = \boldsymbol{\Psi} = \begin{bmatrix} 1 & 0 \end{bmatrix}^T$ yields the unstable reduced order system $\dot{\hat{\boldsymbol{x}}} = \hat{\boldsymbol{x}}$.

A large variety of methods are available to guarantee stable and accurate ROMs of LTI systems defined by Eq. 6.1 [79, 10, 57]. Probably the most common method is balanced truncation. In balanced truncation, the coordinate transformation and projection are carried out using the following

$$\boldsymbol{\Phi} = \begin{bmatrix} \sigma_1^{-1/2} \varphi_1 \\ \vdots \\ \sigma_r^{-1/2} \varphi_r \end{bmatrix} L_o \tag{6.4a}$$

$$\boldsymbol{\Psi}^T = L_c \begin{bmatrix} \psi_1 \sigma_1^{-1/2} & \cdots & \psi_r \sigma_r^{-1/2} \end{bmatrix} \tag{6.4b}$$

where:

- ψ_i are the normalized and ordered eigenvectors of $L_c^T W_o L_c$ and σ_i are square roots of its corresponding eigenvalues.

- φ_i are the normalized and ordered row eigenvectors of $L_o W_c L_o^T$.
- W_o and W_c are the observability and controllability grammians respectively and L_o and L_c are their respective Choleski decompositions .

The observability gramian, W_o and controllability gramian, W_c are unique solutions to the Lyapunov equations $\mathbf{W}_o\mathbf{A}+\mathbf{A}^T\mathbf{W}_o+\mathbf{C}^T\mathbf{C}=0$ and $\mathbf{A}\mathbf{W}_c+\mathbf{W}_c\mathbf{A}^T-\mathbf{B}\mathbf{B}^T=0$ respectively. In addition to guaranteeing ROM stability, balanced truncation offers very favorable and rigorous accuracy bounds. For example, the transfer functions of the original system, G and reduced system, $\hat{G}$ satisfy the following upper bound for error.

$$\left\|G-\hat{G}\right\|_\infty \leqslant 2\sum_{i=n}^{N}\sigma_i \tag{6.5}$$

The two most expensive calculations associated with balanced truncation are finding the Gramians W_o, W_c, and calculating the first n dominant eigenvectors φ_i and ψ. For systems of large dimension these calculations can be prohibitively high. Over the years, several methods of approximate balancing have been developed. Many of these approximate balancing methodologies alleviate computational costs through low rank approximations of the controllability and observability matrices [4, 68, 8, 3, 48, 36] and several of these methods have been applied to linearized fluid flows [54, 78]. The drawback of any gramian based MOR approach however is that often times, not even approximate gramians of the full order model are available. For example, when deriving ROMs from experimental data, sometimes only spatial basis functions derived using POD are available.

A promising new stabilization methodology [2] has recently been proposed that does not rely on approximations of the controllability and observability matrices. In this new approach, the projection matrices, $\mathbf{\Phi}$ and$\mathbf{\Psi}$ are selected from a larger set of candidate basis functions. Let the columns of $\mathbf{\Xi} \in \mathbb{R}^{N_x \times N}$ contain basis functions

derived using a standard data reduction techniques such as POD. In the standard Galerkin MOR approach, the ROMs would be derived using a orthogonal projection, i.e. $\mathbf{\Phi} = \mathbf{\Psi}$ using the first n more "energetic" basis function. In the new proposed stabilization approach [2], the coordinate transformation is fixed $\mathbf{\Phi} = \mathbf{\Xi}(:, 1 : n)$ while the projection matrix is set equal to a subspace of $\mathbf{\Xi}$, i.e $\mathbf{\Psi} = \mathbf{\Xi T}$ where $\mathbf{T} \in \mathbb{R}^{N \times n}$. The matrix $\mathbf{T}$ is linear superposition matrix that governs how the N basis functions in $\mathbf{\Xi}$ are to be superimposed to form the n projection basis functions. The goal in this proposed approach is to find the transformation matrix $\mathbf{T}$ such that the reduced order state matrix $\hat{\mathbf{A}} = \mathbf{T}^T \mathbf{\Xi A \Phi}$ is asymptotically stable, i.e. $\Re\{\hat{\lambda}_i\} < 1$ for $i = 1, \cdots, n$. In [2] the authors formulate the problem as small-scale convex optimization problem using the Lyapunov equation to enforce stability. The advantage of this approach is that any arbitrary basis functions can be utilized and the stabilization procedure operates on the reduced states only.

6.2 Review of stabilization approaches for nonlinear systems

In contrast to linear systems, very few rigorous stabilization methodologies are available for ROMs of nonlinear systems. The methods that do exist are specialized to particular problems [59] and/or are applicable to weakly nonlinear systems only [58]. In fluid flow applications, recent developments include piecewise modeling [52, 28] and nonlinear system identification techniques [63, 7, 6]. In addition, various strategies that can be regarded as reduced order CFD approaches include temporal pseudo-spectral (i.e. harmonic balance) approaches [29] and Petrov–Galerkin approaches [16]. However, for MOR nonlinear fluid flows, the Galerkin-based MOR approach remains the most popular. The drawback of the standard Galerkin-based MOR of the Navier-Stokes is that the derived ROMs are often unstable. In practice, stabilization is achieved a posteriori through addition of auxiliary empirical turbulence models. One of the most widely used approaches is the use of eddy viscosity

models. Over the years many elaborate methods of calibrating eddy viscosities have been proposed [51, 5, 72, 64]. For example, in [18] an empirical viscosity model is calibrated using the energy conservation principle of turbulent Navier-Stokes fluid flows. The following is a summary of this approach.

The canonical form of a ROM of the Navier-Stokes equations that is derived using the standard projection-based MOR approach is as follows

$$\dot{a}_i = \sum_{jk}^{n} Q_{ijk} a_j a_k + \sum_{j}^{n} D_{ij} a_j + b_i \qquad i = 1, \cdots, n \tag{6.6}$$

where variables a_i are the temporal coefficients associated with the standard spectral discretization

$$\boldsymbol{u}(\boldsymbol{x}, t) \approx \boldsymbol{u}^{[0,\cdots,n]} = \boldsymbol{u}_0 + \sum_{i=1}^{n} a_i(t) \boldsymbol{u}_i(\boldsymbol{x}) \tag{6.7}$$

The turbulent kinetic energy, $E(t)$ of the flow is defined as

$$E(t) \equiv \frac{1}{2} \int_{\Omega} |\boldsymbol{u}(\boldsymbol{x}, t)|^2 \, dx \tag{6.8}$$

Because the spatial basis functions used in the spectral discretization are orthonormal, the turbulent kinetic energy corresponding to the i^{th} mode, $E_i(t)$ can be expressed as a function of the temporal coefficients only

$$E_i(t) = \frac{1}{2} a_i(t)^2 \quad i = 1, \cdots, n \tag{6.9}$$

A dynamical equation for the turbulent kinetic energy, $E_i(t)$ is obtained by substituting Eq. (6.6) into the time derivative of $E_i(t)$

$$\dot{E}_i(t) = \frac{d\left(\frac{1}{2} a_i(t)^2\right)}{dt} = a_i(t) \dot{a}_i(t) \quad i = 1, \cdots, n \tag{6.10}$$

Thus, the dynamical equation for $E_i(t)$ is of the form

$$\dot{E}_i(t) = \sum_{jk}^{n} Q_{ijk} a_i a_j a_k + \sum_{j}^{n} D_{ij} a_i a_j + b_i a_i \quad i,j,k = 1, \cdots, n \tag{6.11}$$

For statistically stationary turbulent fluid flows, the time-average of the turbulent kinetic energy associated with each mode is a constant and therefore, the time average of the time derivative of the turbulent kinetic energy is zero, i.e. for stationary turbulent flow $\left\langle \dot{E}_i(t) \right\rangle_T = 0$ for $i = 1, \cdots, n$. The time average of the dynamical equation for $E_i(t)$ is of the form

$$\left\langle \dot{E}_i(t) \right\rangle_T = \sum_{jk}^{n} Q_{ijk} \Upsilon_{ijk} + \sum_{j}^{n} D_{ij} \rho_{ij} + b_i \mu_i \quad i = 1, \cdots, n \tag{6.12}$$

where $\boldsymbol{\Upsilon} \in \mathbb{R}^{n \times n \times n}$, $\rho \in \mathbb{R}^{n \times n}$ and $\boldsymbol{\mu} \in \mathbb{R}^{n \times 1}$ are matrices containing the temporal correlations

$$\Upsilon_{ijk} = \langle a_i a_j a_k \rangle_T \tag{6.13a}$$

$$\rho_{ij} = \langle a_i a_j \rangle_T \tag{6.13b}$$

$$\mu_i = \langle a_i \rangle_T \tag{6.13c}$$

where for POD basis functions $\rho_{ij} = diag\{\lambda_i\}$ and $\mu_i = 0, \forall i$. In general, finite n POD basis functions, a_i and $\boldsymbol{u}_i$ do not satisfy this kinetic energy balance criteria. This is true despite the fact that the POD basis functions optimally reconstruct the time averaged turbulent kinetic energy of the snapshot matrix. The POD algorithm does not take into account the dynamics of system that produced the snapshot matrix. POD works for fluid flows just as well as it does for digital image compression and therefore it is no surprise that the POD basis functions do not satisfy conservation properties of the the dynamical equations. In [18] a linear viscosity, ϑ is added to

correct for the kinetic energy imbalance

$$\left\langle \dot{E}_i(t) \right\rangle_T = \sum_{jk}^{n} Q_{ijk}\Upsilon_{ijk} + \sum_{j}^{n} \left(D_{ij} + \vartheta_{ij}\right)\rho_{ij} + b_i\mu_i \quad i = 1, \cdots, n \tag{6.14}$$

The authors demonstrate this approach using the turbulent flow inside a lid-driven cavity. To achieve ROM stability however, the viscosity parameter, ϑ had to be increased past equilibrium until an appropriate overall dissipation was achieved. In other words, the correct stability criteria is as follows

$$\left\langle \dot{E}_i(t) \right\rangle_T = \sum_{jk}^{n} Q_{ijk}\Upsilon_{ijk} + \sum_{j}^{n} \left(D_{ij} + \vartheta_{ij}\right)\rho_{ij} + b_i\mu_i = -\varepsilon_i \quad i = 1, \cdots, n \tag{6.15}$$

where ε_i are positive scalars. Although ε_i are not known a priori, the small size of the ROM means that an appropriate values can be derived very quickly using iteration.

6.3 A new proposed approach to stabilization of projection-based ROMs of the Navier-Stokes

We propose a new, non-empirical approach to stabilization of projection-based ROMs of the Navier-Stokes equations. The new proposed approach combines the kinetic balance stabilization approach developed in [18] with the basis recombination stabilization approach developed in [2]. As in [18], we attempt to stabilize the ROMs by balancing the kinetic energy. However, in our new proposed approach, we do not use empirical turbulence modeling to achieve the kinetic energy balance. Instead, we utilize the basis recombination method of [18] to find basis functions that satisfy the energy balance a priori. The new proposed methodology is summarized as follows.

Let $\boldsymbol{u}_i(\boldsymbol{x})$ and $a_i(t)$ for $i = 1, \cdots, N$ identify the first N most energetic POD spatial basis functions. Let $\boldsymbol{u}'_i(\boldsymbol{x})$ and $a'_i(t)$ for $i = 1, \cdots, n$ $(N > n)$ identify a set of basis functions that are a superposition of the first N most energetic POD spatial

basis functions. By vectorizing the functions

$$\mathbf{U} = \begin{bmatrix} \boldsymbol{u}_1 & \boldsymbol{u}_2 & \cdots & \boldsymbol{u}_N \end{bmatrix} \tag{6.16a}$$

$$\mathbf{U}' = \begin{bmatrix} \boldsymbol{u}'_1 & \boldsymbol{u}'_2 & \cdots & \boldsymbol{u}'_n \end{bmatrix} \tag{6.16b}$$

$$\mathbf{A} = \begin{bmatrix} a_1 & a_2 & \cdots & a_N \end{bmatrix}^T \tag{6.16c}$$

$$\mathbf{A}' = \begin{bmatrix} a'_1 & a'_2 & \cdots & a'_n \end{bmatrix}^T \tag{6.16d}$$

the relationship between the two sets of basis functions as follows

$$\mathbf{U}' = \mathbf{U}\mathbf{T} \tag{6.17a}$$

$$\mathbf{A}' = \mathbf{T}^T\mathbf{A} \tag{6.17b}$$

where $\mathbf{T} \in \mathbb{R}^{N\times n}$ is the orthonormal ($\mathbf{T}^T\mathbf{T} = \mathbf{I}_{\mathbf{n}\times\mathbf{n}}$) transformation matrix. Thus, we seek a set of basis functions, $\boldsymbol{u}'_i(\boldsymbol{x})$ and $a'_i(t)$ such that the turbulent kinetic energy is balanced

$$\left\langle \dot{E}'_i(t) \right\rangle_T = \sum_{jk}^{n} Q'_{ijk}\Upsilon'_{ijk} + \sum_{j}^{n} D'_{ij}\rho'_{ij} + b'_i\mu'_i = -\varepsilon_i \quad i = 1, \cdots, n \tag{6.18}$$

where $\mathbf{Q}' \in \mathbb{R}^{n\times n\times n}$, $\mathbf{D}' \in \mathbb{R}^{n\times n}$ and $\boldsymbol{b}' \in \mathbb{R}^{n\times 1}$ are the Galerkin matrices associated with the new basis functions, u'_i and $\boldsymbol{\Upsilon}' \in \mathbb{R}^{n\times n\times n}$, $\rho' \in \mathbb{R}^{n\times n}$ and $\boldsymbol{\mu}' \in \mathbb{R}^{n\times 1}$ are matrices containing the temporal correlations

$$\Upsilon'_{ijk} = \left\langle a'_i a'_j a'_k \right\rangle_T \tag{6.19a}$$

$$\rho'_{ij} = \left\langle a'_i a'_j \right\rangle_T \tag{6.19b}$$

$$\mu'_i = \left\langle a'_i \right\rangle_T \tag{6.19c}$$

All terms in Eq. (6.22) can be expressed as a function of POD Galerkin matrices and the transformation matrix $\mathbf{T}$ as follows

$$Q'_{ijk} = \sum_{p=1}^{n} T_{pi} T_{:i}^{T} Q_{p::} T_{:k} \quad i,j,k = 1, \cdots, n \tag{6.20a}$$

$$\mathbf{D}' = \mathbf{T}^{T} \mathbf{D} \mathbf{T} \tag{6.20b}$$

$$\boldsymbol{b}' = \mathbf{T}^{T} \boldsymbol{b} \tag{6.20c}$$

$$\Upsilon'_{ijk} = \sum_{p=1}^{n} T_{pi} T_{:i}^{T} \Upsilon'_{p::} T_{:k} \quad i,j,k = 1, \cdots, n \tag{6.20d}$$

$$\boldsymbol{\rho}' = \mathbf{T}^{T} \boldsymbol{\rho} \mathbf{T} \tag{6.20e}$$

$$\boldsymbol{\mu}' = \mathbf{T}^{T} \boldsymbol{\mu} \tag{6.20f}$$

where for POD basis functions $\rho_{ij} = diag\{\lambda_i\}$ and $\mu_i = 0, \forall i$. Therefore, the new proposed stabilization methodology can be expressed as a nonlinear constrained optimization problem as follows

$$\begin{aligned} &\underset{\mathbf{T} \in \mathbb{R}^{N \times n}}{\operatorname{argmin}} \quad \left\| \sum_{i}^{n} \lambda_i - \sum_{i}^{n} \left(\mathbf{T}^{T} diag\{\lambda\} \mathbf{T} \right)_{ii} \right\| \\ &\text{s. t.} \qquad (1)\ \mathbf{T}^{T} \mathbf{T} = \mathbf{I}_{n \times n} \\ &\qquad\quad (2)\ \left\langle \dot{E}'_i(t) \right\rangle_T + \varepsilon'_i = 0; \end{aligned} \tag{6.21}$$

Minimization of the objective function in Eq. 6.21 ensures that the new basis functions are as close to the optimal POD basis functions as possible. Minimization of the objective function subject to the two constraints ensures the new basis functions are orthonormal (constraint no. 1) and that the new basis functions conserve the balance of turbulent kinetic energy transfer (constraint no. 2). Direct numerical simulation of this $N \times n$ constrained nonlinear minimization problem would be very computationally expensive because the second constraint requires the generation of the nonlinear Galerkin matrices $\mathbf{Q}'$ at each iteration step and is a sextic function of

the transformation matrix $\mathbf{T}$.

Fortunately, for a large class of turbulent flows governed by the incompressible Navier-Stokes equations, the computation of the nonlinear terms can be avoided. It can be shown that the Galerkin matrix $\mathbf{Q}$ is energy preserving, i.e. $\sum_{ijk}^{n} Q'_{ijk} \left\langle a'_i a'_j a'_k \right\rangle_T = 0$ [34, 20, 41]. This nonlinear energy conversation principle holds for many boundary conditions including steady Dirichlet conditions (lid-driven cavity), ambient flow or free-stream conditions at infinity, or periodic boundary conditions. For convective boundary condition (mixing layer), this energy preserving property has not been rigorously proven. However, this conservation principle has been numerically observed to vanish for a variety of simulations including the mixing layer simulation. To take advantage of this symmetry, we must reformulate the second constraint in Eq. (6.21) as a global energy balance. The global turbulent kinetic energy of the flow, $E(t)$ is simply equal to a summation of the modal energies $E(t) = \sum_{i=1}^{n} E_i(t)$. Thus, the global energy balance is of the form

$$\left\langle \dot{E}'(t) \right\rangle_T = \sum_{ijk}^{n} Q'_{ijk} \Upsilon'_{ijk} + \sum_{ij}^{n} D'_{ij} \rho'_{ij} + \sum_{i}^{n} b'_i \mu'_i = -\varepsilon' \tag{6.22}$$

where now, ε' is a single scalar that quantifies the overall dissipation of the global, time-averaged, turbulent kinetic energy of the flow. Since the nonlinear term $\mathbf{Q}$ does not contribute to the over all kinetic energy balance, the stabilization approach can be stated as follows

$$\begin{aligned} \underset{\mathbf{T}\in\mathbb{R}^{\mathbf{N}\times\mathbf{n}}}{\operatorname{argmin}} \quad & \left\| \sum_{i}^{n} \lambda_i - \sum_{i}^{n} \left(\mathbf{T}^T diag\{\lambda\} \mathbf{T} \right)_{ii} \right\| \\ \text{s. t.} \quad & (1)\ \mathbf{T}^T \mathbf{T} = \mathbf{I}_{n\times n} \\ & (2)\ \sum_{ij}^{n} \left(\mathbf{T}^T \mathbf{D} \mathbf{T} \right)_{ij} \left(\mathbf{T}^T diag\{\lambda\} \mathbf{T} \right)_{ij} + \varepsilon' = 0 \end{aligned} \tag{6.23}$$

6.4 The algorithm and numerical implementation

For reasonably small problems, Eq. (6.23) can be directly implemented and solved in MATLAB using the Sequential Quadratic Programming (SQP) method [24, 60, 47] found in MATLAB's constrained nonlinear multivariable minimization package `fmincon`. A MATLAB implementation of this algorithm is provided in Appendix A.4. The following pseudo-code summarizes the approach.

Algorithm 1 Stabilization Algorithm

Input: POD basis functions, $\boldsymbol{u}_i(\boldsymbol{x})$ and $a_i(t)$ for $i = 1, \cdots, N$ and the associated Galerkin matrices $\mathbf{Q} \in \mathbb{R}^{N\times N\times N}$, $\mathbf{D} \in \mathbb{R}^{N\times N}$ and $\boldsymbol{b} \in \mathbb{R}^{N\times 1}$. The global dissipation parameter ε',

Output: Galerkin-based ROM [$\mathbf{Q'} \in \mathbb{R}^{n\times n\times n}$, $\mathbf{D'} \in \mathbb{R}^{n\times n}$,$\boldsymbol{b'} \in \mathbb{R}^{n\times 1}$] associated with the transformed basis functions, $\boldsymbol{u}'_i = \sum_j^N T_{ji}\boldsymbol{u}_j$ for $i = 1, \cdots, n$ and $j = 1, \cdots, N$

1: Choose $n > 0$, s.t. $N > n$

2: Compute POD eigenvalues $\lambda_i = \langle a_i a_i \rangle_T$

3: Solve the optimization problem:

$$\begin{aligned} \underset{\mathbf{T}\in\mathbb{R}^{\mathbf{N}\times\mathbf{n}}}{\operatorname{argmin}} \quad & \left\| \sum_i^n \lambda_i - \sum_i^n \left(\mathbf{T}^T diag\{\lambda\}\mathbf{T}\right)_{ii} \right\| \\ \text{s. t.} \quad & (1)\ \mathbf{T}^T\mathbf{T} = \mathbf{I}_{n\times n} \\ & (2)\ \sum_{ij}^n \left(\mathbf{T}^T\mathbf{D}\mathbf{T}\right)_{ij} \left(\mathbf{T}^T diag\{\lambda\}\mathbf{T}\right)_{ij} + \varepsilon' = 0 \end{aligned} \tag{6.24}$$

4: Compute Galerkin matrices:

$$Q'_{ijk} = \sum_{p=1}^n T_{pi} T_{:i}^T Q_{p::} T_{:k} \quad i, j, k = 1, \cdots, n \tag{6.25a}$$

$$\mathbf{D'} = \mathbf{T}^T\mathbf{D}\mathbf{T} \tag{6.25b}$$

$$\boldsymbol{b'} = \mathbf{T}^T\boldsymbol{b} \tag{6.25c}$$

5: Compute $\boldsymbol{u}'_i = \sum_j^N T_{ji}\boldsymbol{u}_j$ for $i = 1, \cdots, n$ and $j = 1, \cdots, N$

6: Return $\boldsymbol{u}'_i$, $\mathbf{T}$ and stabilized ROM [$\mathbf{Q'} \in \mathbb{R}^{n\times n\times n}$, $\mathbf{D'} \in \mathbb{R}^{n\times n}$,$\boldsymbol{b'} \in \mathbb{R}^{n\times 1}$]

7

Stabilized Reduced Order Models (ROMs)

In this section the new proposed stabilization methodology is used to derive projection based ROMs of the lid-driven cavity and the mixing layer. In Section 7.4 the turbulent kinetic energy balance is calculated exactly, i.e $\varepsilon' = 0$. The results in this section demonstrate that balancing the turbulent kinetic energy does not, in general, produce stable ROMs. Stabilization requires basis functions that are on average more dissipative. In Section 7.4 the stabilization methodology is iterated until the appropriate overall dissipation is found.

The stabilization minimization problem is solved in MATLAB using the the constrained nonlinear multivariable minimization package `fmincon`. A MATLAB implementation of this algorithm is provided in Appendix A.4. The function evaluation tolerance, `TolFun` and constraint tolerance, `TolCon` are both set to 1×10^{-9}. In all simulations demonstrated in this thesis, suitable solutions are found in fewer than 100 iterations.

7.1 Stabilization using exact turbulent kinetic energy balance $\varepsilon' = 0$

Figures 7.1 and Figures 7.2 illustrate the evolution of the turbulent kinetic energy of ROMs of the lid-driven cavity. Figures 7.1 and 7.2 correspond to ROM orders n = 1,2,3 and n = 10,20,50 respectively. The thick black curves correspond to the standard POD-Galerkin ROMs that, as expected, are all unstable. The dashed black curves correspond to ROMs derived using the new proposed stabilization methodology. The stabilized ROMs are all derived using a superposition of the first $N = 100$ POD basis functions and the stabilized ROMs are all derived using an exact balance of the kinetic energy, i.e. $\varepsilon' = 0$. In Figures 7.1 and Figures 7.2 the DNS is identified by the thick gray curves, the optimal reconstructions using the standard POD basis functions are identified by the thin red curves while the optimal reconstructions using the new energy preserving basis functions functions are identified by the dashed blue curves. The standard POD ROMs are identified by the dashed black curves while the stabilized ROMs are identified by the solid black curves. *Stabilization using an exact balance of kinetic energy, $\varepsilon' = 0$ performs well at stabilizing the small order ROMs while having limited influence on the higher order ROMs.*

Finally, note the proximity of the two sets of optimal reconstructions; there is no visible difference between the dashed blue line that corresponds to the optimal reconstruction using the new basis functions and the thin red line that corresponds to the optimal reconstruction using the POD basis functions. Satisfying the kinetic energy balance constraint requires very little modification to the POD basis function. In other words, the transformation matrix resembles the following

$$\mathbf{T}_{N\times n} = \begin{bmatrix} \mathbf{I}_{n\times n} \\ \mathbf{0}_{(N-n)\times n} \end{bmatrix} + \delta_{N\times n} \tag{7.1}$$

where $\mathbf{I}_{n\times n}$ and $\mathbf{0}_{(N-n)\times n}$ are the identity and null matrices respectively. $\delta_{N\times n}$ is a matrix whose entries are all less than one, i.e. $\delta_{ij} < 1$ for $i = 1, \cdots, N$ and

$j = 1, \cdots, n$. This proximity of the two sets of basis functions is summarized in Table 7.1. Table 7.1 contains the optimal time-averaged, turbulent kinetic energy captured by the first n POD basis functions, $\boldsymbol{u}_i$ and the first n basis functions, $\boldsymbol{u}'_i$ derived using the new proposed stabilization methodology with $\varepsilon' = 0$. The

n	$\tilde{E}$	$\tilde{E}'$, $\varepsilon' = 0$
1	16.12	16.03
2	29.34	29.24
3	37.61	37.52
10	67.16	67.06
20	82.40	82.25
50	93.60	93.52

Table 7.1: Percentage of turbulent kinetic energy of the lid-driven cavity captured by the first n POD basis functions vs. the first n stabilized basis functions.

percentaged of time-averaged, turbulent kinetic energy captured by the first n basis functions, $\boldsymbol{u}'_i$ is labeled, $\tilde{E}'$ and defined as follows

$$\tilde{E}' = \frac{\langle E'_{OPT}(t) \rangle_T}{\langle E_{DNS}(t) \rangle_T} \times 100 = \frac{\sum_{i=1}^{n} \lambda'_i}{\sum_{i=1}^{N} \lambda_i} \times 100 \tag{7.2}$$

where $diag\{\lambda'_i\} = \mathbf{T}^T diag\{\lambda_i\}\mathbf{T}$.

Figures 7.3 and Figures 7.4 illustrate the evolution of the turbulent kinetic energy of ROMs of the mixing layer. Figures 7.3 and 7.4 correspond to ROM orders n = 1,2,3 and n = 11,20,50 respectively. Results for the mixing layer are similar to the lid-driven cavity; the standard ROMs are all unstable and the stabilization using an exact balance of kinetic energy, $\varepsilon' = 0$ only stabilizes the low-order ROMs. Also, as before, the two sets of basis functions are very similar; there is no visible difference between the dashed blue line that corresponding to the optimal reconstruction using the new basis functions and the thin red line that corresponds to the optimal reconstruction using the POD basis functions.

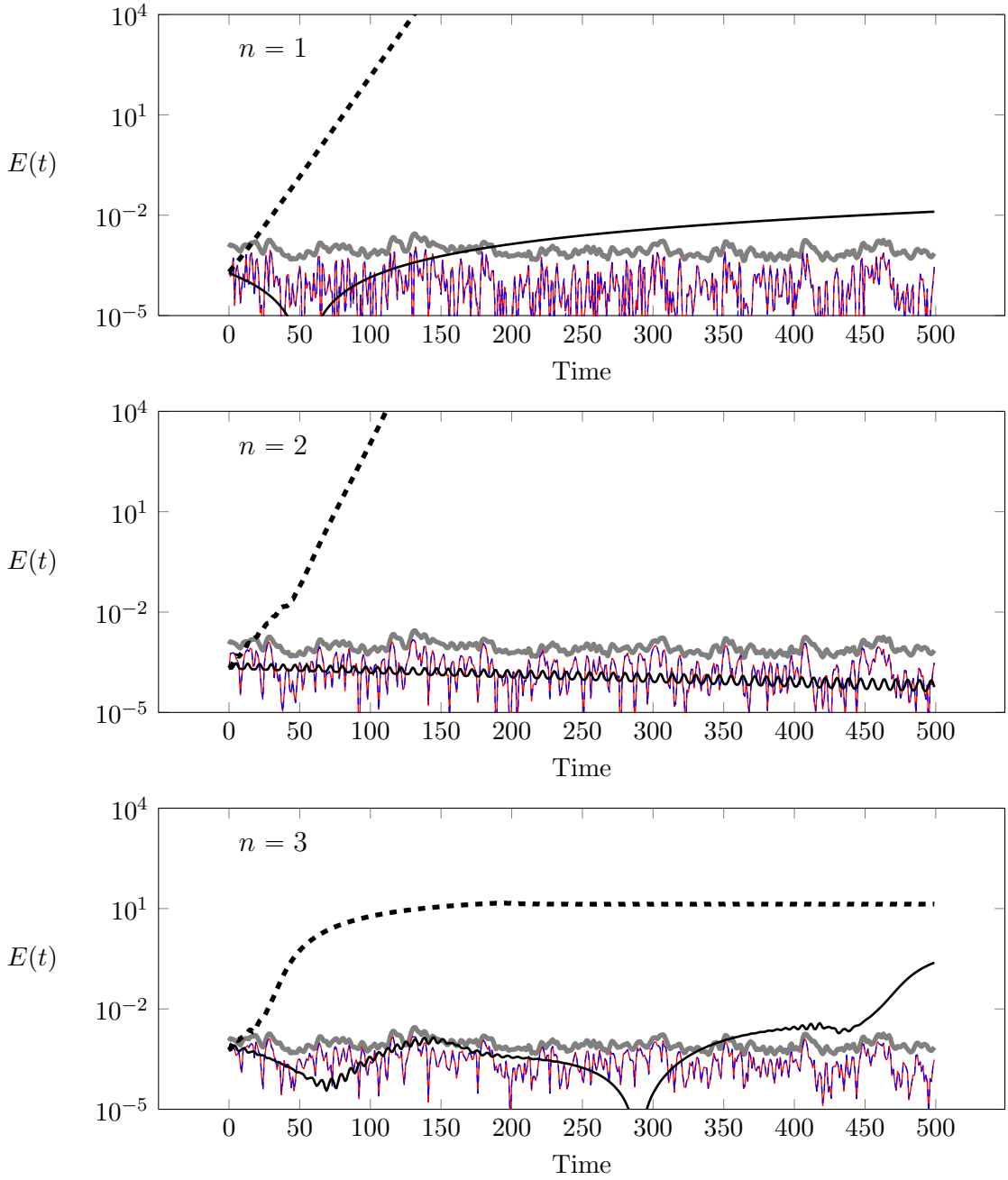

FIGURE 7.1: Evolution of the turbulent kinetic energy of the lid driven cavity as predicted by the DNS: $E_{DNS}(t)$(▬), the optimal reconstruction using the POD basis functions: $E_{OPT}(t)$(——) and the optimal reconstruction using the stabilized basis functions: $E'_{OPT}(t)$(- - -). Integration of the standard POD-Galerkin ROM: $E_{ROM}(t)$(▪▪▪) and the integration of a stabilized ROM: $E'_{ROM}(t)$(——). The stabilized ROMs are derived using an exact energy balance, $\varepsilon' = 0$ using a superposition of $N = 100$ POD basis functions.

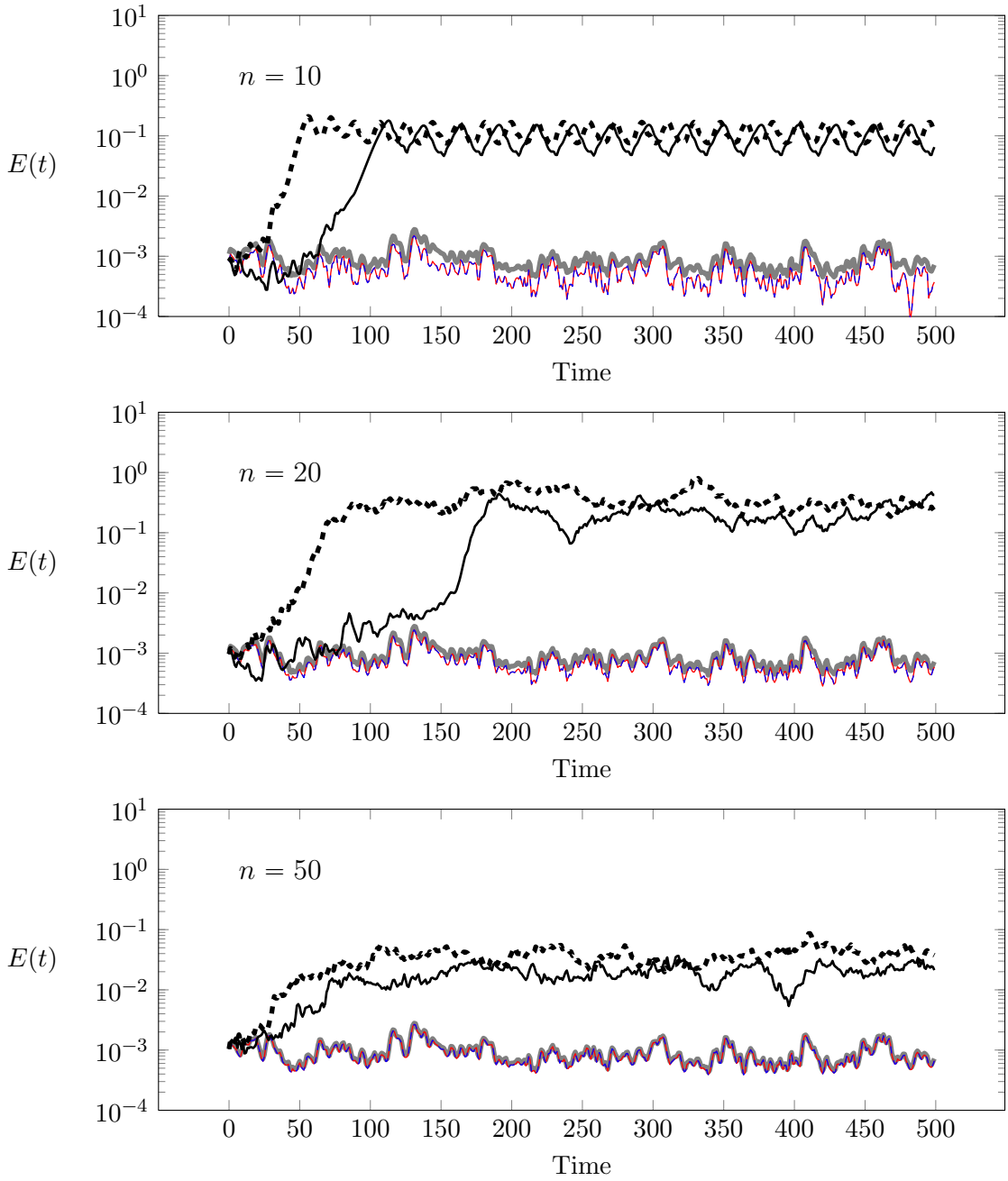

FIGURE 7.2: Evolution of the turbulent kinetic energy of the lid driven cavity as predicted by the DNS: $E_{DNS}(t)$(▬), the optimal reconstruction using the POD basis functions: $E_{OPT}(t)$(——) and the optimal reconstruction using the stabilized basis functions: $E'_{OPT}(t)$(- - -). Integration of the standard POD-Galerkin ROM: $E_{ROM}(t)$(▪▪▪) and the integration of a stabilized ROM: $E'_{ROM}(t)$(——). The stabilized ROMs are derived using an exact energy balance, $\varepsilon' = 0$ using a superposition of $N = 100$ POD basis functions.

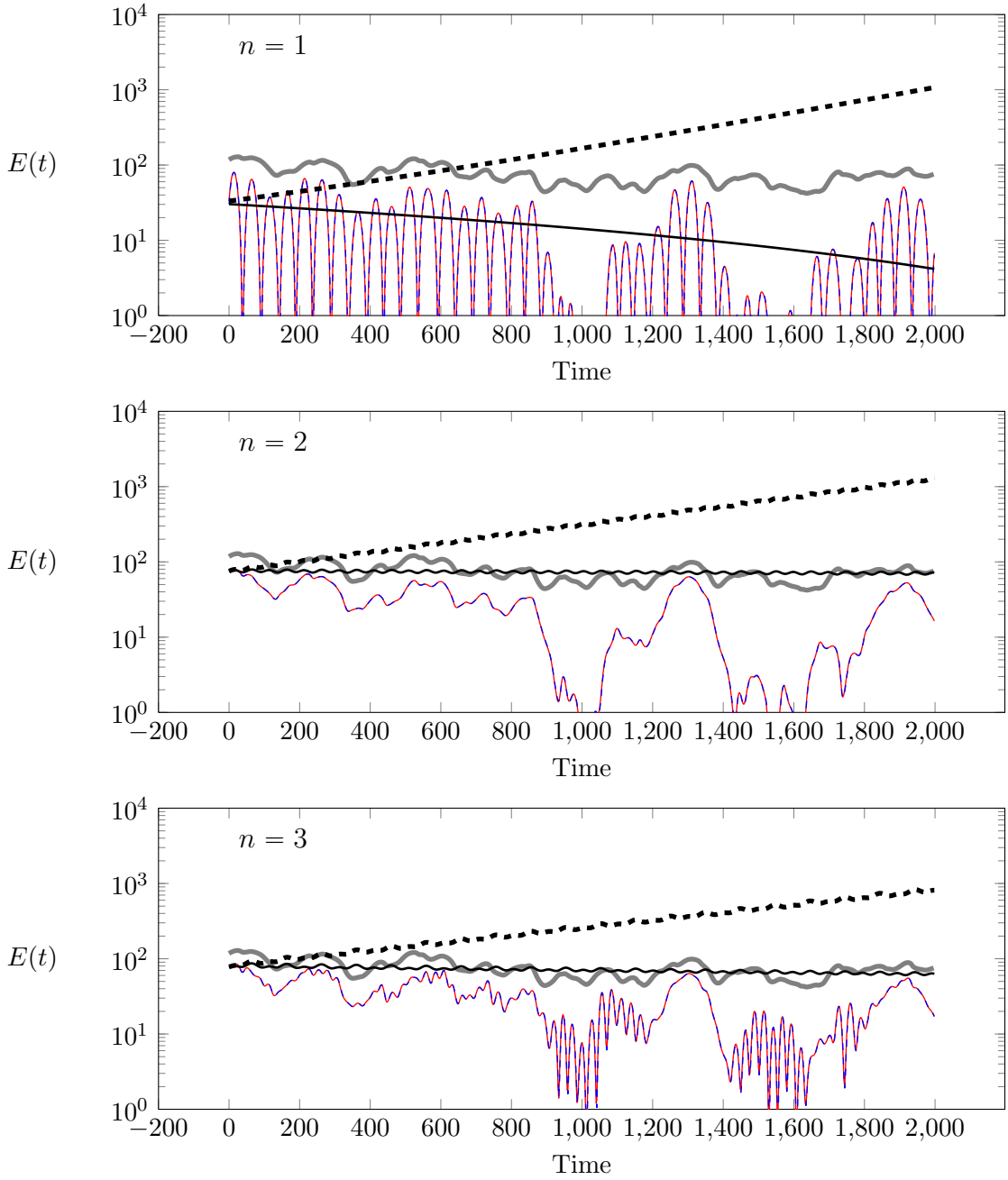

FIGURE 7.3: Evolution of the turbulent kinetic energy of the mixing layer as predicted by the DNS: $E_{DNS}(t)$(▬), the optimal reconstruction using the POD basis functions: $E_{OPT}(t)$(——) and the optimal reconstruction using the stabilized basis functions: $E'_{OPT}(t)$(- - -). Integration of the standard POD-Galerkin ROM: $E_{ROM}(t)$(▪▪▪) and the integration of a stabilized ROM: $E'_{ROM}(t)$(——). The stabilized ROMs are derived using an exact energy balance, $\varepsilon' = 0$ using a superposition of $N = 100$ POD basis functions.

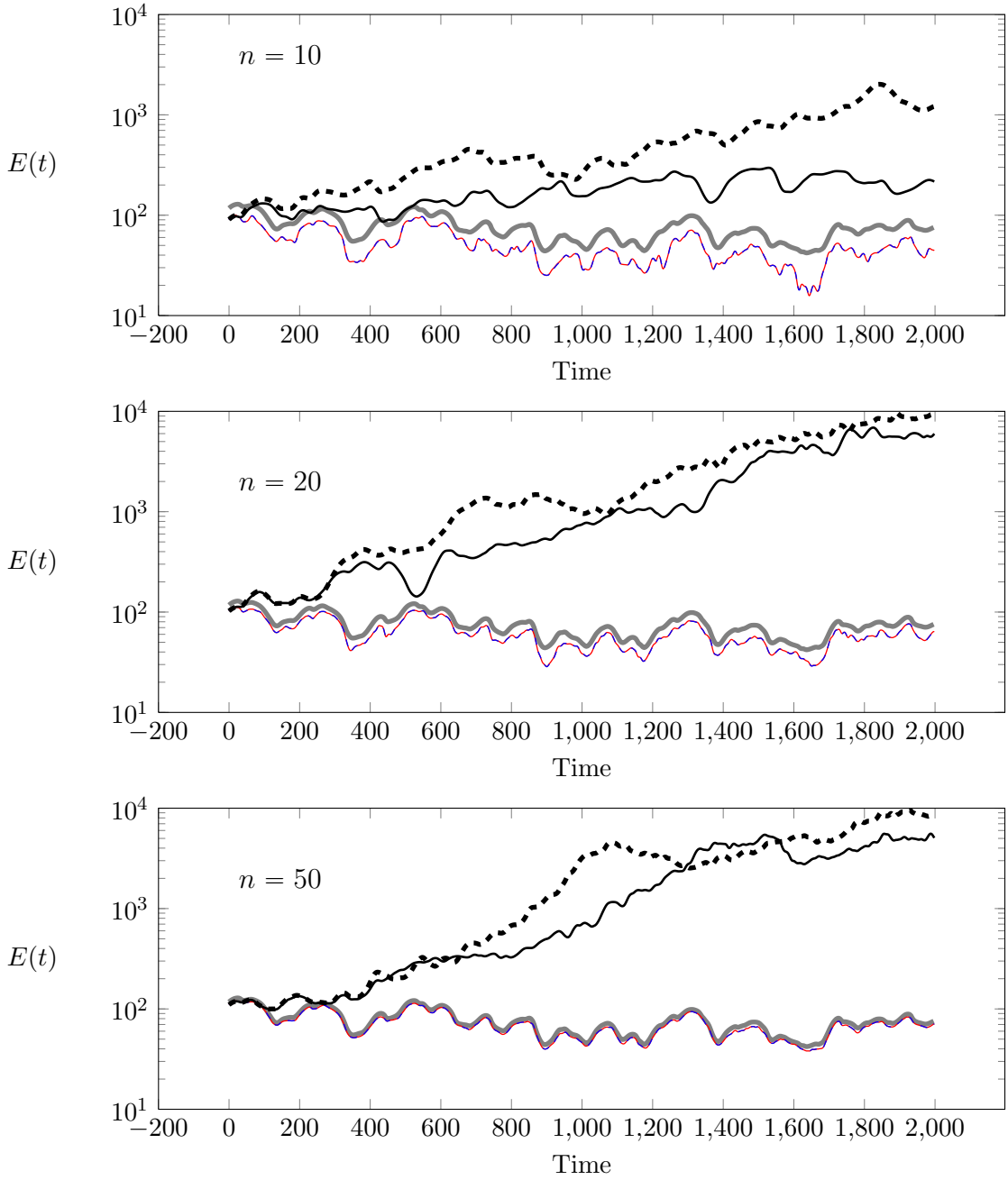

FIGURE 7.4: Evolution of the turbulent kinetic energy of the mixing layer as predicted by the DNS: $E_{DNS}(t)$(▬), the optimal reconstruction using the POD basis functions: $E_{OPT}(t)$(——) and the optimal reconstruction using the stabilized basis functions: $E'_{OPT}(t)$(- - -). Integration of the standard POD-Galerkin ROM: $E_{ROM}(t)$(▪▪▪) and the integration of a stabilized ROM: $E'_{ROM}(t)$(——). The stabilized ROMs are derived using an exact energy balance, $\varepsilon' = 0$ using a superposition of $N = 100$ POD basis functions.

The proximity of the two sets of basis functions for the mixing layer is summarized in Table 7.2. Table 7.2 contains the optimal time-averaged, turbulent kinetic energy captured by the first n POD basis functions, $\boldsymbol{u}_i$ and the first n basis functions, $\boldsymbol{u}'_i$ derived using the new proposed stabilization methodology using $\varepsilon' = 0$.

n	$\tilde{E}$	$\tilde{E}'$, $\varepsilon' = 0$
1	18.35	18.34
2	35.27	35.25
3	40.87	40.85
10	66.80	66.77
20	81.77	81.75
50	95.50	95.47

Table 7.2: Percentage of turbulent kinetic energy of the mixing layer captured by the first n POD basis functions vs. the first n stabilized basis functions.

7.2 Stabilization using $\varepsilon' = \varepsilon'_{stab}$

In Section 7.4 it was demonstrated that ROMs derived using basis functions for which $\sum_{ij}^{n} \left(\mathbf{T}^T\mathbf{D}\mathbf{T}\right)_{ij} \left(\mathbf{T}^T diag\{\lambda\}\mathbf{T}\right)_{ij} = 0$ were in general not stable. In this section we conjecture that stable ROMs can be derived using basis function for which the global time averaged, kinetic energy is dissipative; basis functions for which $\sum_{ij}^{n} \left(\mathbf{T}^T\mathbf{D}\mathbf{T}\right)_{ij} \left(\mathbf{T}^T diag\{\lambda\}\mathbf{T}\right)_{ij} + \varepsilon'_{stab} = 0$ where ε'_{stab} is a positive scalar. To the best of the authors' knowledge, it is not possible to derive ε'_{stab} a priori. We propose the following simple iterative approach. Given the initial condition, $\varepsilon'_0 = 0$ solve the stabilization algorithm (1) and integrate the derived ROM for a predefined time interval. If the ROM is stable, i.e. $\langle E'_{ROM}(t)\rangle_T = \langle E'_{OPT}(t)\rangle_T$, return $\varepsilon'_{stab} = \varepsilon'_0$ and exit. If the ROM is unstable, increase $\varepsilon'_n = \varepsilon'_{n-1} + \Delta\varepsilon'$ and repeat until stabilization is achieved. The most expensive calculation in this iterative scheme is the

generation and integration of the ROM for each value of ε'_n. Since the computational costs associated with generating and integrating a Galerkin-based ROM increase very quickly with order n, this proposed iterative scheme is only practical for small ROMs $(N, n < 50)$. Our experience is that the stabilization is robust to the number of POD basis function, N. Our experience suggests $N \approx 2n$ as a good rule of thumb.

Figures 7.5 illustrate the evolution of the turbulent kinetic energy of ROMs of the lid-driven cavity. The dashed black curves correspond to the standard POD-Galerkin ROMs that, as expected, are all unstable. The solid black curves correspond to ROMs derived using the new proposed stabilization methodology using $\varepsilon' = 0$. Finally, the green curves corresponds to ROMs derived using $\varepsilon' = \varepsilon'_{stab}$. Figure 7.6 illustrates the Power Spectral Density (PSD) of the turbulent kinetic energy as predicted by ROM derived using $\varepsilon' = \varepsilon'_{stab}$. The PSD is estimated using Welch's averaged, modified periodogram method [77]. Specifically, MATLAB's built-in Welch's algorithm, `cpsd` is utilized. The estimating is performed using a Hamming window with a 50% overlap. The length of the Hamming window is such that eight equal sections of the signal are used to compute the average. Figure 7.6 illustrates how the dynamics of the stabilized ROMs converge to the DNS as the order of the model is increased. As before, the stabilized basis functions are very close to the original POD basis functions as summarized in Table 7.3. Finally, Figure 7.7 illustrates the kinetic energy balance, ε'_{stab} required to stabilize the ROMs. Aside from the fact that ε'_{stab} is positive for all orders n, no clear trend is visible.

The results for the mixing layer flow are very similar to the lid-driven cavity as illustrated in Figures 7.8. The standard POD-Galerkin ROMs of the mixing layer, identified by the dashed black curves, are all unstable. The solid black curves correspond to ROMs derived using the new proposed stabilization methodology using $\varepsilon' = 0$. Finally, the green curves corresponds to ROMs derived using $\varepsilon' = \varepsilon'_{stab}$. The dynamics of the stabilized ROMs converge to the DNS of the lid-driven cavity as

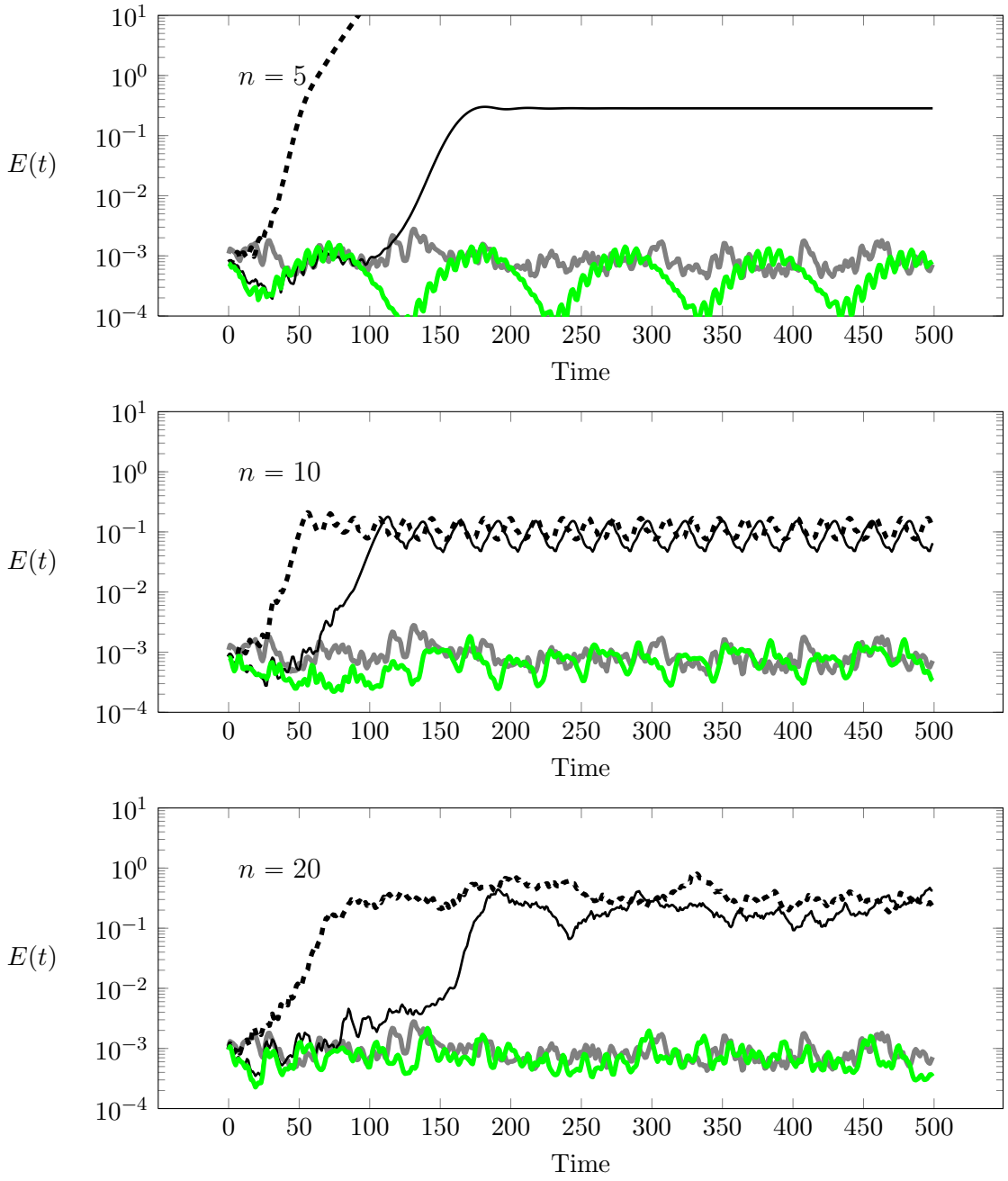

FIGURE 7.5: Evolution of the turbulent kinetic energy of the lid driven cavity as predicted by the DNS(▬), the standard POD-Galerkin ROM(▪▪▪), stabilized ROMs using $\varepsilon' = 0$ (——) and stabilized ROMs using $\varepsilon' = \varepsilon'_{stab}$ (▬).

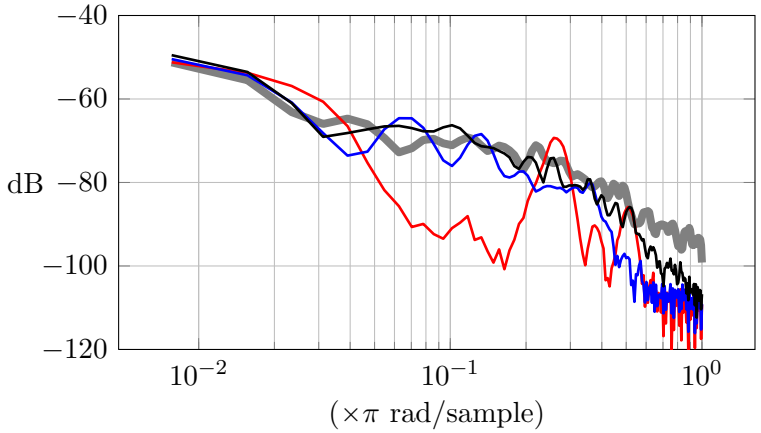

FIGURE 7.6: PSD of the turbulent kinetic energy of the lid driven cavity as predicted by the DNS (▬) and stabilized ROMs using $\varepsilon' = \varepsilon'_{stab}$ of order $n = 5$ (—), 10 (—) and 20 (—).

n	$\tilde{E}$	$\tilde{E}'$, $\varepsilon' = 0$	$\tilde{E}'$, $\varepsilon' = \varepsilon_{stab}$
5	50.37	50.19	50.01
10	67.16	67.06	66.72
20	82.40	82.25	82.11

Table 7.3: Percentage of turbulent kinetic energy of the lid-driven cavity captured by the first n POD basis functions vs. the first n stabilized basis functions.

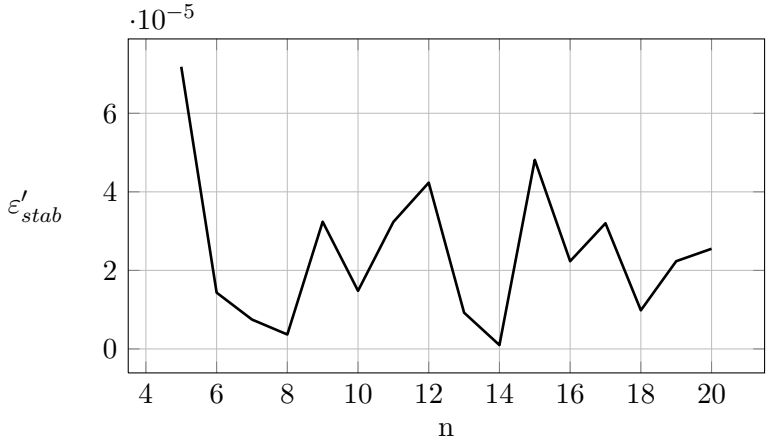

FIGURE 7.7: Kinetic energy balance of stabilized ROMs of the lid driven cavity.

the order of the model is increased. Figure 7.9 illustrates the PSD of the turbulent kinetic energy as predicted by ROM derived using $\varepsilon' = \varepsilon'_{stab}$. Figure 7.9 illustrates how the dynamics of the stabilized ROMs converge to the DNS as the order of the model is increased. As before, the stabilized basis functions are very close to the original POD basis functions as summarized in Table 7.4. Finally, Figure 7.10 illustrates the kinetic energy balance, ε'_{stab} required to stabilize the ROMs. Similarly to the lid-driven cavity, no clear trend in ε'_{stab} is visible.

n	$\tilde{E}$	$\tilde{E}'$, $\varepsilon' = 0$	$\tilde{E}'$, $\varepsilon' = \varepsilon'_{stab}$
5	50.71	50.70	50.21
10	66.80	66.77	66.67
20	81.77	81.75	79.14

Table 7.4: Percentage of turbulent kinetic energy of the mixing layer captured by the first n POD basis functions vs. the first n stabilized basis functions.

7.3 Reconstruction of the full flow field

In this section the temporal coefficients, $a'_i(t)$ derived from integration of the stabilized ROMs are used to reconstruct the the full flow field of the lid-driven cavity and mixing layer. The full flow field is reconstructed using the standard spectral discretization

$$\boldsymbol{u}(\boldsymbol{x},t) \approx \boldsymbol{u}^{[0,\cdots,n]} = \boldsymbol{u}_0 + \sum_{i=1}^{n} a'_i(t)\boldsymbol{u}'_i(\boldsymbol{x}) \tag{7.3}$$

where $\boldsymbol{u}_0$ is the temporal mean. Figure 7.11 illustrates the vorticity contours of the lid-driven cavity as predicted by the DNS, the optimal reconstruction using the stabilized basis functions and the reconstruction derived from a numerical integration of the stabilized ROM. The predicted flow field of the lid-driven cavity predicted by the ROM appears qualitatively similar to the optimal. Because the ROM equations are generally chaotic, similarity can only be expected in a statistical sense. Finally,

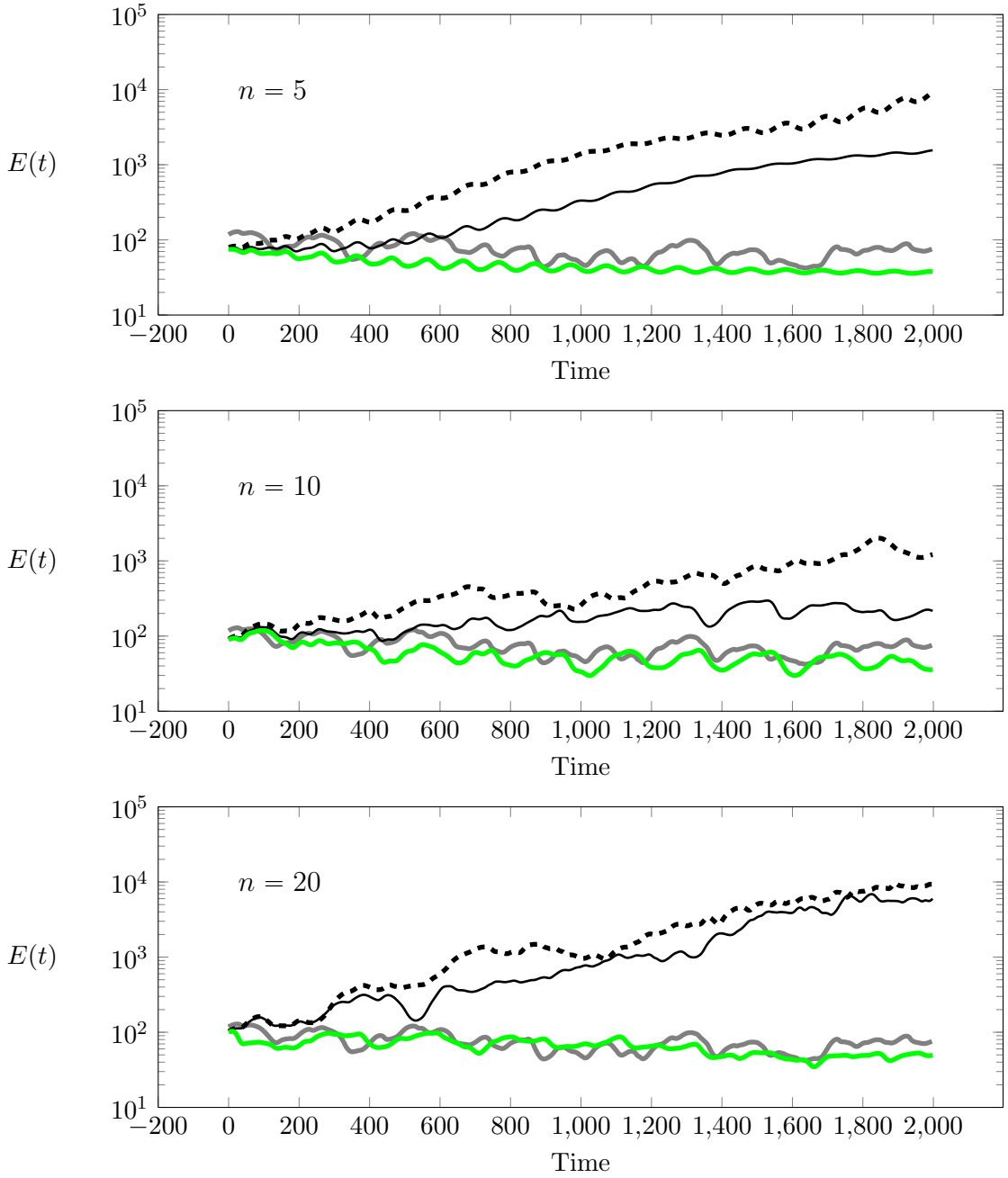

FIGURE 7.8: Evolution of the turbulent kinetic energy of the mixing layer as predicted by the DNS(▬), the standard POD-Galerkin ROM(▪▪▪), stabilized ROMs using $\varepsilon' = 0$ (—) and stabilized ROMs using $\varepsilon' = \varepsilon'_{stab}$ (▬).

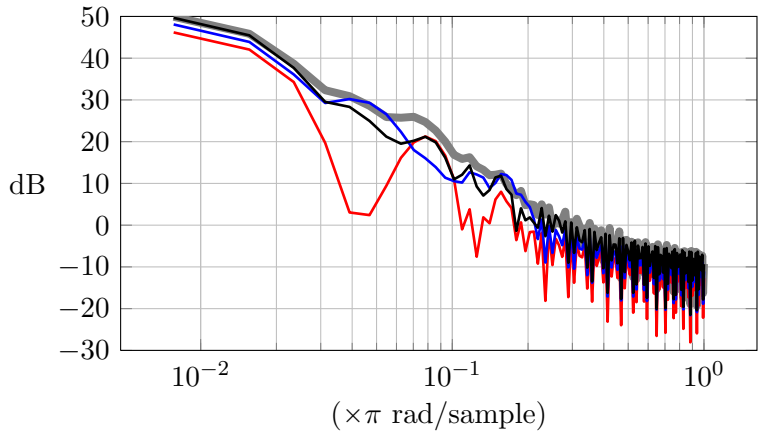

FIGURE 7.9: PSD of the turbulent kinetic energy of the mixing layer as predicted by the DNS (▬) and stabilized ROMs using $\varepsilon' = \varepsilon'_{stab}$ of order $n = 5$ (—), 10 (—) and 20 (—).

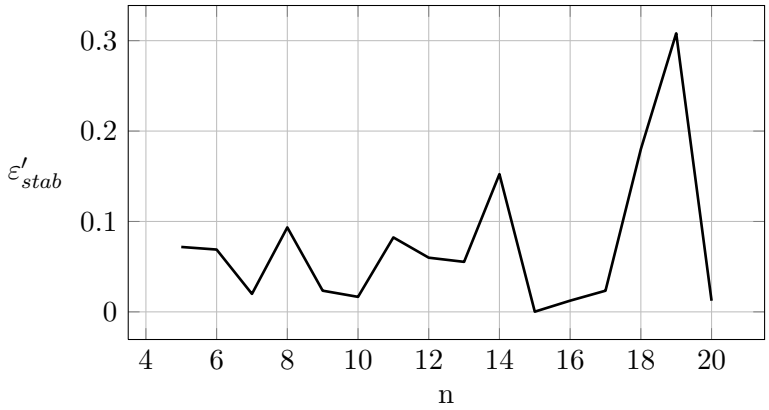

FIGURE 7.10: Kinetic energy balance of stabilized ROMs of the mixing layer.

Figure 7.12 illustrates the vorticity contours of the mixing layer at $t = 1000$. Similarly to the lid-driven cavity, the ROM reconstruction of the mixing layer flow is qualitatively similar to the optimal reconstruction.

7.4 Robustness of stabilized ROMs to changes in Reynolds number

In this section, the stabilized ROMs are used to predict the flow at a Reynolds number that is different from the one used to derive and stabilize ROMs. Specifically, we predict the turbulent kinetic energy inside the lid-driven cavity at $\mathrm{Re_u} = 4 \times 10^4$

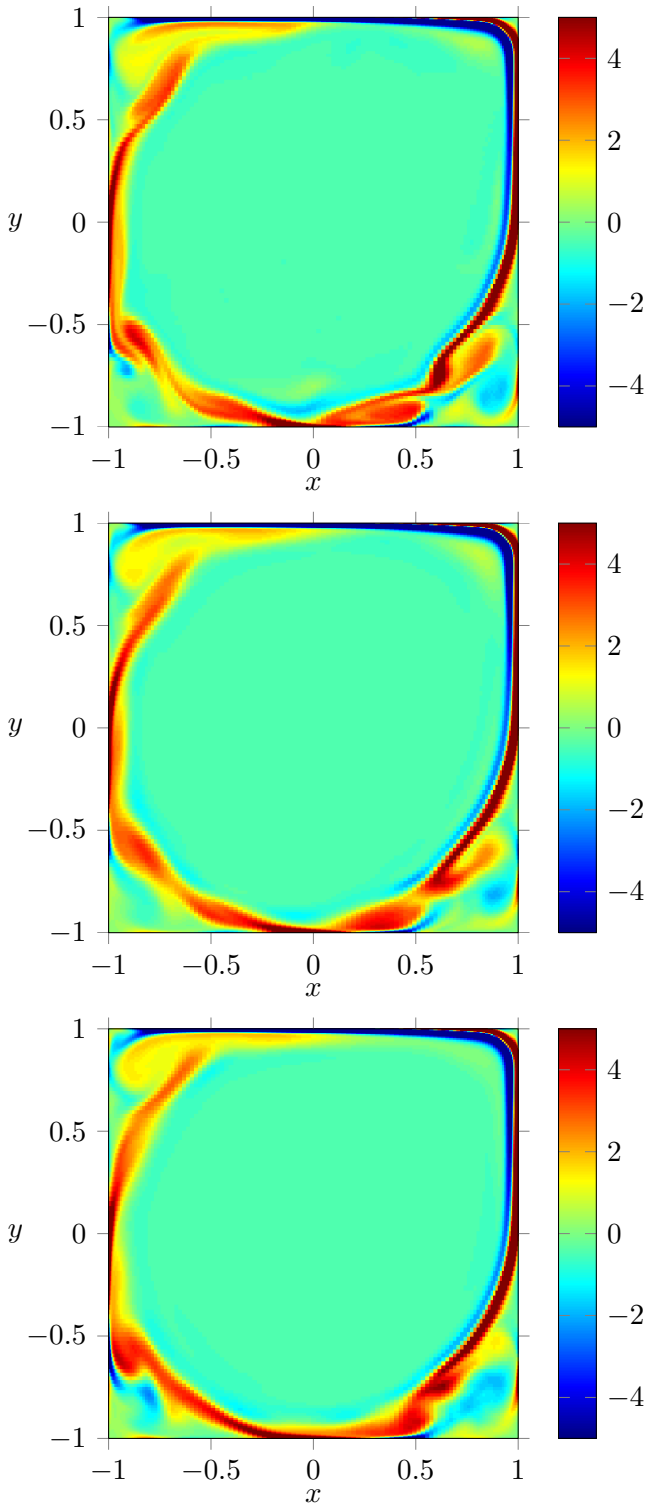

FIGURE 7.11: Reconstructions of the vorticity field of the lid-driven cavity at $t = 200$ using the $n = 20$, $\varepsilon' = \varepsilon_{stab}$ stabilized ROM. The top subfigure corresponds to the DNS simulation, the middle subfigure corresponds to the optimal reconstruction using the stabilized basis function, u_i' and a_i' and the bottom subfigure corresponds to the reconstruction derived from a numerical integration of the stabilized ROM.

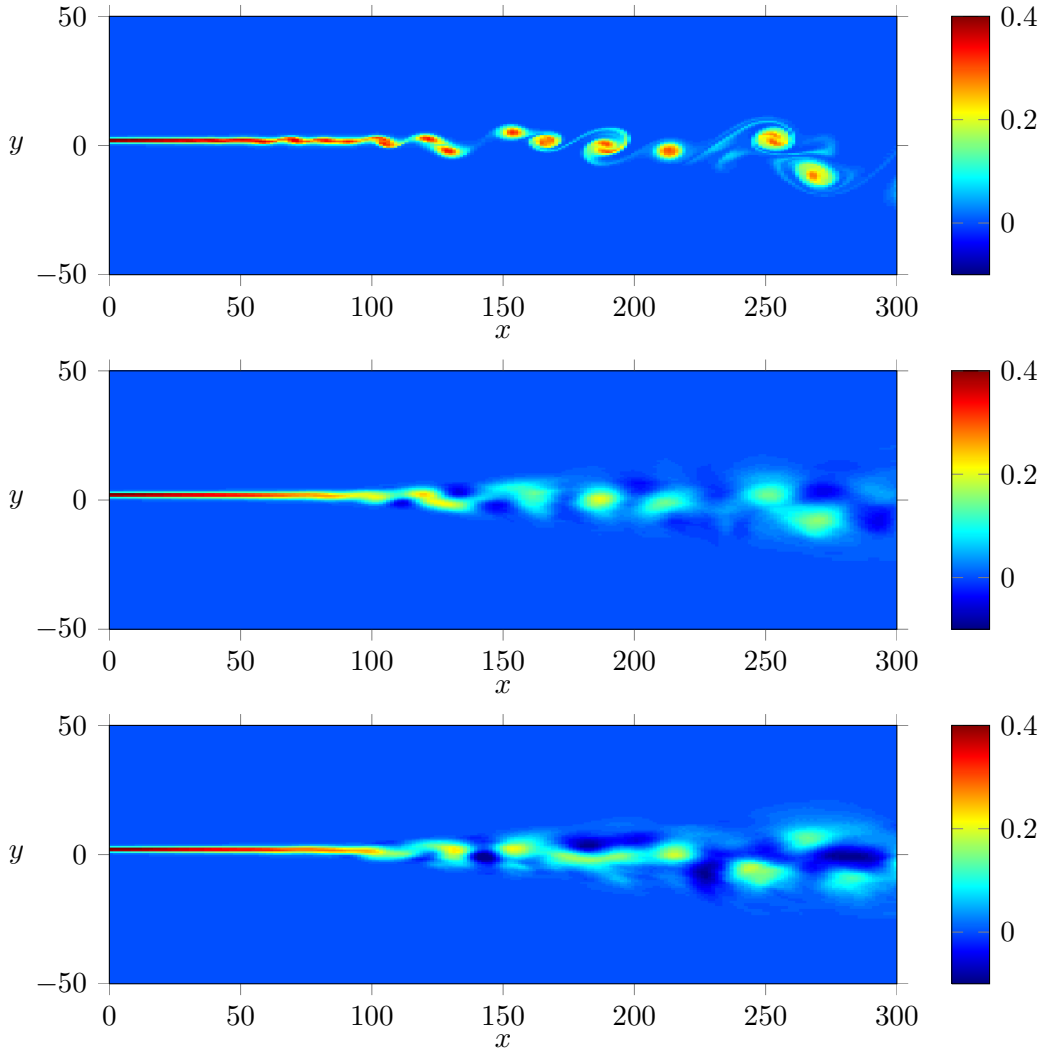

FIGURE 7.12: Reconstructions of the vorticity field of the mixing layer at $t = 1000$ using the $n = 20$, $\varepsilon' = \varepsilon_{stab}$ stabilized ROM. The top subfigure corresponds to the DNS simulation, the middle subfigure corresponds to the optimal reconstruction using the stabilized basis function, u_i' and a_i' and the bottom subfigure corresponds to the reconstruction derived from a numerical integration of the stabilized ROM.

and $\mathrm{Re_u} = 2.5 \times 10^4$ using a ROM that was derived and stabilized using the flow at $\mathrm{Re_u} = 3 \times 10^4$. Figure 7.13 illustrates the evolution of the turbulent kinetic energy of the lid-driven cavity at these three Reynolds number as predicted using DNS. As expected, the overall magnitude of the turbulent kinetic energy is proportional to the Reynolds number.

To quantify ROM accuracy, we use the following percent relative error

$$\%Error = \frac{\langle E'_{OPT}(t)\rangle_T - \langle E'_{ROM}(t)\rangle_T}{\langle E'_{OPT}(t)\rangle_T} \times 100 \tag{7.4}$$

where as before, $\langle E'_{OPT}(t)\rangle_T = \sum_{i=1}^{N} \lambda'_i$. However this time, the POD eigenvalues are with respect to the flow at a different Reynolds number. To calculate these eigenvalues the optimal temporal coefficients, a'_i associated with the basis functions, u'_i for the new flow must be evaluated. Since the spatial basis functions are orthonormal, the optimal temporal coefficients are $a'_i(t) = \langle u'_i(x), u_s(x,t)\rangle_\Omega$ where u_s is the snapshot of the flow field at the new Reynolds number. Finally, the optimal eigenvalues equal $\lambda'_i = \langle a'_i(t), a'_i(t)\rangle_T$. Table 7.5 summarizes the performance of the stabilized ROMs in predicting the flow at the two new Reynolds numbers. *The percent error decreases as as the order or the ROMs is increased.*

n	$\mathrm{Re_u} = 2.5 \times 10^4$	$\mathrm{Re_u} = 3.0 \times 10^4$	$\mathrm{Re_u} = 4.0 \times 10^4$
5	-854%	0.92%	123%
10	69.0%	0.55% %	-213%
20	-7.10%	-0.89%	13.6%

Table 7.5: Percent error of stabilized ROMs in predicting flows at different Reynolds numbers.

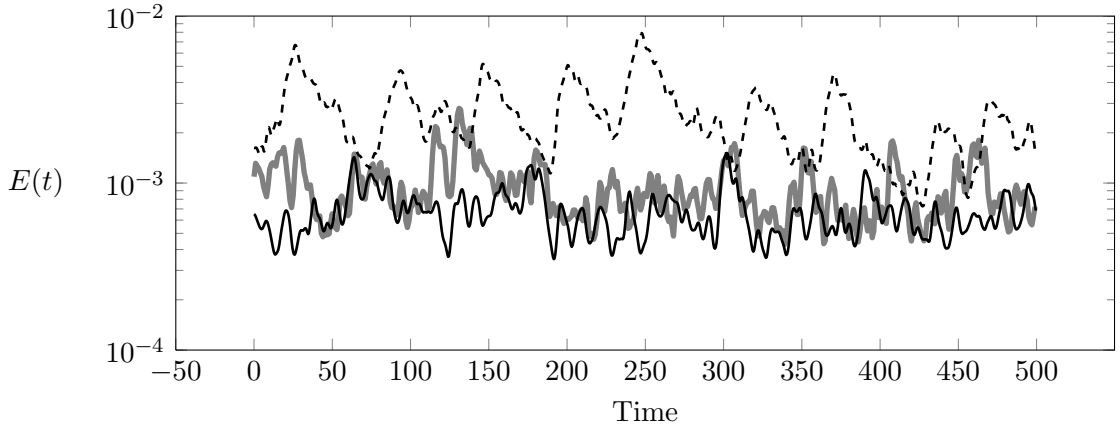

FIGURE 7.13: Evolution of the turbulent kinetic energy of the lid driven cavity as predicted by the DNS at $\mathrm{Re_u} = 3{\times}10^4$(▬), $\mathrm{Re_u} = 2.5{\times}10^4$(——) and $\mathrm{Re_u} = 4.0{\times}10^4$ (- - -).

8

Conclusions

This chapter contains a summary of the contributions of this thesis, along with suggestions for future work.

8.1 Summary

Chapter 2 discussed the general projection-based Model Order Reduction (MOR) approach for dynamical systems. Specifically, a summary of the spectral method and Galerkin projection was presented including how these methods may be used together to form a Reduced Order Model (ROM) of the Navier-Stokes equations. The standard projection-based MOR approach yields ROMs that are a set of coupled quadratic Ordinary Differential Equations (ODEs) for the temporal coefficients of the spectral discretization. The stability and accuracy of these ROMs is quantified using the turbulent kinetic energy of the fluid flow.

Chapter 3 discusses the two test cases used in this thesis: the two-dimensional flow inside a square lid-driven cavity and the two-dimensional mixing layer. The boundary conditions and flow parameters of both test cases are discussed and details of the numerical solvers used to produce Direct Numerical Simulations (DNS)

summarized. Typical vorticity snapshots of the fluid flows are presented and the turbulent kinetic energy of the flows is calculated.

Chapter 4 discusses the Proper Orthogonal Decomposition (POD) of the two test cases. The vorticity contours of several POD spatial and temporal basis functions are illustrated. The spatial and temporal characteristics of these basis functions demonstrate the universal characteristics of turbulent flows: Large physical scales are associated with low frequency temporal dynamics while small physical scales are associated with high frequency temporal dynamics.

Chapter 5 discusses the stability characteristics and convergence properties of POD projection-based ROMs of the Navier-Stokes equations. Despite the fact that POD basis functions are the optimal basis functions to reconstruct the turbulent kinetic energy of the fluid flow, the ROMs derived using the POD basis functions are unstable for small to moderate numbers of POD basis functions. Convergence to the DNS solution is achieved only if a large number of POD basis functions is utilized. Achieving convergence in this way is not always practical because the associated ROMs are large and therefore expensive to solve computationally.

In Chapter 6 a new proposed stabilization methodology to projection-based ROMs of the Navier-Stokes equations is introduced. The chapter begins with a discussion on rigorous stabilization approaches for ROMs of finite dimensional, Linear Time Invariant (LTI) systems. In contrast to linear systems, very few rigorous stabilization methodologies are available for ROMs of nonlinear systems. For nonlinear fluid flows, projection-based ROMs are stabilized empirically through the addition of empirical turbulence modeling. To achieve ROM stability, the empirical turbulence models must be adjusted until the right balance of dissipation is achieved. The drawback of this stabilization approach is that the empirical turbulence models modify the dynamics of the Navier-Stokes equations. The goal of the new, non-empirical stabilization methodology is to find a set of basis functions different from the standard

POD basis functions that model the correct balance of ROM dissipation a priori. The new proposed stabilization approach is formulated as a small-sized, nonlinear constrained minimization problem. At the end of this chapter, an algorithm for solving the minimization problem is introduced and its numerical implementation in MATLAB is presented.

In Chapter 7 the new proposed stabilization approach is used to derive ROMs of the two test cases. The accuracy and stability of the derived ROMs is quantified using the turbulent kinetic energy of the flows. The stabilized ROMs are also used to reconstruct the full flow fields of both test cases. Finally, the stabilized ROMs are used to predict flows at Reynolds numbers different from the Reynolds number used to create the ROM models.

8.2 Future work

There are several possible avenues for future work; some of these are summarized below.

The new proposed stabilization methodology achieves ROM stability through the utilization of spatial basis functions that are more dissipative than the standard POD spatial basis functions. The overall dissipation of the basis functions is measured using ε' which is the global, time-averaged rate-of-change of the turbulent kinetic energy. The value of ε' for which ROM stability is achieved is not known a priori. This critical value of ε', which we label ε'_{stab}, must be found iteratively. For each value of ε', a ROM must be generated and integrated in time numerically. For small order ROMs, i.e. $n < 20$, this is not an problem because generating and integrating small order ROMs is computationally inexpensive. Iteration becomes very expensive however when larger sized ROMs are used. For example, the generation and numerical integration of a $n = 100$ order ROM of the mixing layer required

approximately 17 hours of CPU time. In order for the proposed stabilization approach to be applicable to large order ROMs, an efficient method of predicting ROM stability would have be to be developed.

The new proposed stabilization methodology is formulated as a nonlinear constrained minimization problem. Minimization of the objective function ensures that the new basis functions are as close to the optimal POD basis functions as possible while the constraints ensure that the new basis functions are orthonormal and balanced to the overall dissipation of ε'. It may be possible to improve the modeling performance of the stabilized ROMs by additional constraints to the stabilization problem. For example, currently, the overall dissipation of the ROM is measured using the global rate-of-change of the turbulent kinetic energy. The global turbulent kinetic energy of the flow, $E(t)$ is simply equal to a summation of the modal energies $E(t) = \sum_{i=1}^{n} E_i(t)$. It is possible that ROM performance could be improved by controlling how each of the modes contribute to the overall kinetic energy balance.

The two dimensional lid-driven cavity and the mixing layer are good prototypical example problems of turbulent Navier-Stokes flows. However, the methodology must be validated using three-dimensional Navier-Stokes fluid flow. In principle this should be possible since nowhere during the development of the proposed methodology was two-dimensionality assumed and/or required. In addition, flows at higher Reynolds numbers should be also be investigated.

Appendix A

Matlab code

A.1 Proper orthogonal decomposition

The following is a MATLAB code for the POD decomposition of a snapshot matrix `X`. The inputs of the function, `POD` are the snapshot matrix, `X` $\in \mathbb{R}^{N_x \times N_t}$, the number of POD basis functions, `N` and the matrix, `dx` $\in \mathbb{R}^{N_x \times 1}$ that contains the size of the discretized volume elements. N_x is the number of states of the system and N_t is the number of temporal samples of these states. The states of the system are stored in the rows of `X` and the columns of `X` correspond the values of the states at different times The function, `POD` outputs the POD spatial basis functions, `U` $\in \mathbb{R}^{N_x \times N}$, the POD temporal functions, `A`$\in \mathbb{R}^{N \times N_t}$ and the POD eigenvalues, `lambda` $\in \mathbb{R}^{N \times 1}$. The i^{th} column of the matrix `U` corresponds to the i^{th} POD spatial basis function while the i^{th} row of the matrix `A` corresponds to the i^{th} POD temporal basis function

```
function [U,A,lambda]=POD(X,N,dx)
    mean_X = mean(X,2);
    X = bsxfun(@minus, X, mean_X);
    C = (1/X_t)*X'*bsxfun(@times, X, dx);
    [Uc, Sc, Vc] = svd(C,'econ');
    e = Uc(:,1:N);

    U = X*(e/sqrt(X_t*Sc(1:N,1:N)));
    lambda = sqrt(Sc(1:N,1:N));
    V = e*sqrt(X_t)';
    A = diag(lambda*V');
end
```

A.2 Numerical implementation of inner products

The spatial inner product is approximated using the standard Euclidean norm

$$\langle \boldsymbol{u}_i, \boldsymbol{u}_j \rangle_\Omega = \sum_{k,m} u_i(x_k, y_m) u_j(x_k, y_m) \Delta x_k \Delta y_m \tag{A.1}$$

The following MATLAB code outputs the Galerkin matrices $\mathbf{Q} \in \mathbb{R}^{\mathbf{n}\times\mathbf{n}\times\mathbf{n}}$, $\mathbf{D} \in \mathbb{R}^{\mathbf{n}\times\mathbf{n}}$ and $\boldsymbol{b} \in \mathbb{R}^{n\times 1}$. The `n` spatial basis functions `u` and `v` are sorted as cell arrays. The mean modes are stored as matrices `u_o` and `v_o`. The matrix `dx`$\in \mathbb{R}^{n\times n}$ contains the discrete volumes $\Delta x_k \Delta y_m$. The user defined functions `diff_x()` and `diff_y()` compute the first spatial derivatives in the x and y directions respectively.

```
function [Q,D,b] = Galerkin_Matrices(u,v,u_o,v_o,n,dx,nu)
u_o_x==diff_x(u_o); v_o_x=diff_x(u_o);
u_o_y==diff_y(u_o); v_o_y=diff_y(u_o);
u_o_xx==diff_x(u_o_x); v_o_xx=diff_x(v_o_x);
u_o_yy==diff_y(u_o_y); v_o_yy=diff_y(v_o_y);
u_x==diff_x(u); v_x=diff_x(u);
u_y==diff_y(u); v_y=diff_y(u);
u_xx==diff_x(u_x); v_xx=diff_x(u_x);
u_yy==diff_y(u_y); v_yy=diff_y(u_y);

Q = cell(n,1);
parfor  i = 1:n
for  j = 1:n
for  k = 1:n
Q{i}(j,k)=-sum(sum(dx.*u{i}.*(u{j}.*u_x{k} + v_{j}.*u_y{k}) + ...
```

```
                    dx.*v{i}.*(u{j}.*v_x{k} + v_{j}.*v_y{k}) ...
                              ));
end
end
end

D = zeros(n,n);
parfor  i = 1:n
for  j = 1:n
D(i,j)=sum(sum(nu*dx.*u{i}.*(u_xx{j} + u_yy{j}) + ...
                nu*dx.*v{i}.*(v_xx{j} + v_yy{j}) + ...
               -(  dx.*u{i}.*(u_o.*u_x{j} + v_o.*u_y{j}) + ...
                   dx.*v{i}.*(u_o.*v_x{j} + v_o.*v_y{j}) + ...
                   dx.*u{i}.*(u{j}.*u_o_x + v{j}.*u_o_y) + ...
                   dx.*v{i}.*(u{j}.*v_o_x + v{j}.*v_o_y)        )));

end
end

b = zeros(n,1);
parfor  i=1:n
b(i,1)=sum(sum(nu*dx.*u{i}.*(u_o_xx + u_o_yy) + ...
                nu*dx.*v{i}.*(v_o_xx + v_o_yy) + ...
                -(  dx.*u{i}.*(u_o.*u_o_x + v_o.*u_o_y) + ...
                    dx.*v{i}.*(u_o.*v_o_x + v_o.*v_o_y)        )));
end
end
```

A.3 Numerical integration of Galerkin ROMs

The ROMs generated from Galerkin projection of the Navier-Stokes are integrated numerically in MATLAB using the built-in adaptive forth/fifth order Runge-Kutta scheme `ODE45`. Details for the implementation are available in the MATLAB documentation files and further details are available in [25]. The following MATLAB code integrates for the temporal coefficients `a` due to initial conditions `a(:,1)` in the time interval `[0:d_t:t_max]`.

```
[t,a] = ode45(@(t,a)Galerkin_NS(a,n,Q,D,b),[0:d_t:t_max],a(:,1));
```

The following MATLAB function contains the Galerkin ROM of the Navier-Stokes

```
function da = Galerkin_NS(a,b,Q,D,b)
da = zeros(n,1);
    for i=1:n
        da(i) = a'*Q{i}*a + D(i,:)*a + b(i,1);
    end
end
```

A.4 Solution of the stabilization problem

The following is a MATLAB code that solves the stabilization problem introduced in Chapter 6. The inputs of the function `stabilizeROM` are the `N` spatial, `u` and temporal, `a` POD basis function and the $N \times N$ linear Galerkin matrix `D`. The function stabilizeROM outputs the transformation matrix, `T` and matrices containing the stabilized spatial, `u_tilda` and temporal `a_tilda` basis functions. The objective function, `objective` evaluates the difference between the optimal reconstructions of the time-averaged, turbulent kinetic energy using the POD basis functions and the new basis functions. The constraint function `constraint` functions evaluates the kinetic energy imbalance.

```
function [T,u_tilda,a_tilda] = stabilizeROM(u,a,D,N,n)
    global lambda D

    for i=1:n;
        lambda(i) = mean(a(i,:).*a(i,:));
    end

    x0 = eye(n,n);
    x0(N,:) = 0;

    problem = createOptimProblem('fmincon',...
                'objective', @objective, ...
                'nonlcon', @constraint, ...
                'x0',x0);
    [x,fval,EXITFLAG,OUTPUT,LAMBDA] = fmincon(problem)
    OUTPUT.message

    T=x*(x'*x)^(-1/2);
    u_tilda=u*T;
    a_tilda=T'*a;
end
```

```
function [f] = objective(x)
global lambda;
    T = x*(x'*x)^(-1/2);
    sum_lambda = sum(lambda);
    lambda_tilda = diag(T'*diag(lambda)*T);
    sum_lambda_tilda = sum(lambda_tilda);

    f = sum_lambda - sum_lambda_tilda;
end
```

```
function [c,ceq] = constraint(x)
global D lambda epsilon_stab;
    T=x*(x'*x)^(-1/2);
    D_tilda = T'*D*T;
    lambda_tilda = (T'*diag(lambda)*T);
    ceq = sum(sum(D_tilda.*lambda_tilda)) + epsilon_stab;
    c = [];
end
```

The following is a sample matlab output message for a $N = 10$ and $n = 2$ solution

```
x =
    0.9993    0.0001
    0.0001    0.9996
    0.0044    0.0464
   -0.0056   -0.0084
    0.0563   -0.0799
   -0.0640   -0.0317
    0.0199   -0.0138
    0.0404   -0.0368
   -0.0751    0.0344
    0.0783    0.0159


fval =
   5.0963e-07
EXITFLAG =
     1
OUTPUT =
         iterations: 3
          funcCount: 84
       lssteplength: 1
           stepsize: 1.1044e-05
          algorithm: 'medium-scale: SQP, Quasi-Newton, line-search'
      firstorderopt: 1.8685e-08
    constrviolation: 2.4451e-10
            message: [1x787 char]
LAMBDA =
         lower: [20x1 double]
         upper: [20x1 double]
         eqlin: [1x0 double]
      eqnonlin: 2.2569e-08
        ineqlin: [1x0 double]
    ineqnonlin: [1x0 double]


ans =

Local minimum found that satisfies the constraints.

Optimization completed because the objective function is ...
    non-decreasing in feasible directions, to within the selected ...
    value of the function tolerance, and constraints are ...
    satisfied to within the selected value of the constraint ...
    tolerance.

Stopping criteria details:

```

```
44 Optimization completed: The first-order optimality measure, ...
       1.868486e-08, is less than options.TolFun = 1.000000e-06, and ...
       the maximum constraint violation, 2.445092e-10, is less than ...
       options.TolCon = 1.000000e-06.
45
46 Optimization Metric                                    Options
47 first-order optimality =   1.87e-08         TolFun =   1e-06 ...
       (selected)
48 max(constraint violation) =   2.45e-10      TolCon =   1e-06 ...
       (selected)
```

Bibliography

[1] D. Amsallem and C. Farhat. Interpolation method for adapting reduced-order models and application to aeroelasticity. *AIAA Journal*, 46(7):1803–1813, 2008.

[2] D. Amsallem and C. Farhat. Stabilization of projection-based reduced-order models. *International Journal for Numerical Methods in Engineering*, 2012.

[3] A. Antoulas. *Approximation of large-scale dynamical systems*, volume 6. Society for Industrial Mathematics, 2005.

[4] A. Antoulas, D. Sorensen, and S. Gugercin. A survey of model reduction methods for large-scale systems. *Contemporary mathematics*, 280:193–220, 2001.

[5] N. Aubry, P. Holmes, J. LUMLEY, and E. Stone. The dynamics of coherent structures in the wall region of a turbulent boundary layer. *Journal of Fluid Mechanics*, 192(115):173355, 1988.

[6] M. Balajewicz and E. Dowell. Reduced order modeling of transonic flutter and limit cycle oscillations using the sparse volterra series. *Journal of Aircraft*, 2012.

[7] M. Balajewicz, F. Nitzsche, and D. Feszty. Application of multi-input volterra theory to nonlinear multi-degree-of-freedom aerodynamic systems. *AIAA Journal*, 48(1):56–62, January 2010.

[8] V. Balakrishnan, Q. Su, and C. Koh. Efficient balance-and-truncate model reduction for large scale systems. In *American Control Conference, 2001. Proceedings of the 2001*, volume 6, pages 4746–4751. IEEE, 2001.

[9] M. F. Barone, I. Kalashnikova, D. J. Segalman, and H. K. Thornquist. Stable galerkin reduced order models for linearized compressible flow. *J. Comput. Phys.*, 228(6):1932–1946, Apr. 2009.

[10] J. Bay. *Fundamentals of linear state space systems*. WCB/McGraw-Hill, 1999.

[11] M. Bergmann, C. Bruneau, and A. Iollo. Enablers for robust pod models. *Journal of Computational Physics*, 228(2):516 – 538, 2009.

[12] C. Bogey. *Calcul direct du bruit aérodynamique et validation de modèles acoustiques hybrides*. PhD thesis, Ecole Centrale Lyon, 2000.

[13] J. P. Boyd. *Chebyshev and Fourier Spectral Methods*. Dover, second edition, 2001.

[14] C. Canuto, M. Y. Hussaini, A. Quarteroni, and T. A. Zang. *Spectral Methods in Fluid Dynamics*. Springer, 1991.

[15] C. Canuto, M. Y. Hussaini, A. Quarteroni, and T. A. Zang. *Spectral Methods: Fundamentals in Single Domains*. Springer, 2006.

[16] K. Carlberg, C. Bou-Mosleh, and C. Farhat. Efficient non-linear model reduction via a least-squares petrov–galerkin projection and compressive tensor approximations. *International Journal for Numerical Methods in Engineering*, 86(2):155–181, 2011.

[17] A. Cavalieri, G. Daviller, P. Comte, P. Jordan, G. Tadmor, and Y. Gervais. Using large eddy simulation to explore sound-source mechanisms in jets. *J. Sound Vib.*, 330:4098–4113, 2011.

[18] W. Cazemier, R. W. C. P. Verstappen, and A. E. P. Veldman. Proper orthogonal decomposition and low-dimensional models for driven cavity flows. *Physics of Fluids*, 10(7):1685–1699, 1998.

[19] T. Colonius, S. Lele, and P. Moin. Direct computation of the sound generated by two-dimensional shear layer. In *AIAA, Aeroacoustics Conference, 15 th, Long Beach, CA*, 1993.

[20] L. Cordier, B. Noack, G. Daviller, J. Delvile, G. Lehnasch, G. Tissot, M. Balajewicz, and R. Niven. Control-oriented model identification strategy. *Experiments in Fluids (Submitted manuscript)*, 2012.

[21] M. Couplet, C. Basdevant, and P. Sagaut. Calibrated reduced-order pod-galerkin system for fluid flow modelling. *Journal of Computational Physics*, 207(1):192 – 220, 2005.

[22] W. Daviller. *Numerical study of temperature effects in single and coaxial jets*. PhD thesis, cole nationale suprieure de mcanique et d'arotechnique, 2010.

[23] J. W. Demmel. *Applied Numerical Linear Algebra*. SIAM, 1997.

[24] L. Dixon and G. Szegö. *Towards global optimisation: proceedings of a workshop at the University of Cagliari, Italy, October 1974*. North Holland, 1975.

[25] J. Dormand and P. Prince. A family of embedded runge-kutta formulae. *Journal of computational and applied mathematics*, 6(1):19–26, 1980.

[26] B. Galletti, C. Bruneau, L. Zannetti, and A. Iollo. Low-order modelling of laminar flow regimes past a confined square cylinder. *Journal of Fluid Mechanics*, 503(161170):1, 2004.

[27] D. Gottlieb and E. Turkel. Dissipative two-four method for time dependent problems. *Math. of Comp.*, 30(136):703–723, 1976.

[28] D. Gratton and K. Wilcox. Reduced-order, trajectory piecewise-linear models for nonlinear computational fluid dynamics. In *5th SMA Symposium*, 2004.

[29] K. Hall, J. Thomas, and W. Clark. Computation of unsteady nonlinear flows in cascades using a harmonic balance technique. *AIAA journal*, 40(5):879–886, 2002.

[30] M. E. Hayder and E. Turkel. High-order accurate solutions of viscous problem. In *AIAA paper 93-3074*, 1993.

[31] P. Holmes, J. Lumley, and G. Berkooz. *Turbulence, Coherent Structures, Dynamical Systems and Symmetry*. Cambridge University Press, 1996.

[32] D. Joseph. Stability of fluid motions. i, ii. Technical report, 1976.

[33] G. E. Karniadakis and S. J. Sherwin. *Spectral/hp Element Methods for Computational Fluid Dynamics*. Oxford University Press, USA, 2005.

[34] R. Kraichnan and S. Chen. Is there a statistical mechanics of turbulence? *Physica D: Nonlinear Phenomena*, 37(1-3):160–172, 1989.

[35] O. Ladyzhenskaia, R. Silverman, and J. Chu. *The mathematical theory of viscous incompressible flow*. Gordon & Breach, 1969.

[36] J. Li. *Model reduction of large linear systems via low rank system gramians*. PhD thesis, Massachusetts Institute of Technology, 2000.

[37] G. Lodato, P. Domingo, and L. Vervisch. Three-dimensional boundary conditions for direct and large-eddy simulation of compressible viscous flows. *J. Comp. Phys.*, 227(10):5105–5143, 2008.

[38] P. Moin and K. Mahesh. Direct numerical simulation: A tool in turbulence research. *Annual Review of Fluid Mechanics*, 30:539–578, 1998.

[39] B. Noack, K. Afanasiev, M. Morzynski, G. Tadmor, and F. Thiele. A hierarchy of low-dimensional models for the transient and post-transient cylinder wake. *Journal of Fluid Mechanics*, 497(1):335–363, 2003.

[40] B. Noack and H. Eckelmann. A global stability analysis of the steady and periodic cylinder wake. *Journal of Fluid Mechanics*, 270:297–330, 1994.

[41] B. Noack, M. Morzynski, and G. Tadmor. *Reduced-Order Modelling for Flow Control*. CISM International Centre for Mechanical Sciences. Springer, 2011.

[42] B. Noack, P. Papas, and P. Monkewitz. The need for a pressure-term representation in empirical galerkin models of incompressible shear flows. *Journal of Fluid Mechanics*, 523(1):339–365, 2005.

[43] B. Noack, M. Schlegel, M. Morzynski, and G. Tadmor. System reduction strategy for galerkin models of fluid flows. *International Journal for Numerical Methods in Fluids*, 63:231–248, 2010.

[44] B. R. Noack and R. K. Niven. Maximum-entropy closure for a galerkin model of an incompressible periodic wake. *Journal of Fluid Mechanics*, 700:187–213, 2012.

[45] B. R. Noack, M. Schlegel, B. Ahlborn, G. Mutschke, M. Morzynski, P. Comte, and G. Tadmor. A finite-time thermodynamics of unsteady fluid flows. *J. Non-Equilibr. Thermodyn.*, 33:103–148, 2008.

[46] B. R. Noack, M. Schlegel, M. Morzynski, and G. Tadmor. System reduction strategy for galerkin models of fluid flows. *International Journal for Numerical Methods in Fluids*, 63(2):231–248, 2010.

[47] J. Nocedal and S. Wright. *Numerical optimization*. Springer verlag, 1999.

[48] T. Penzl. Algorithms for model reduction of large dynamical systems. 1999.

[49] M.-L. Rapun and J. M. Vega. Reduced order models based on local pod plus galerkin projection. *Journal of Computational Physics*, 229(8):3046 – 3063, 2010.

[50] D. Rempfer. On low-dimensional galerkin models for fluid flow. *Theoretical and Computational Fluid Dynamics*, 14:75–88, 2000.

[51] D. Rempfer and H. Fasel. Dynamics of three-dimensional coherent structures in a flat-plate boundary layer. *Journal of Fluid Mechanics*, 275:257–284, 1994.

[52] M. Rewienski and J. White. A trajectory piecewise-linear approach to model order reduction and fast simulation of nonlinear circuits and micromachined devices. *Computer-Aided Design of Integrated Circuits and Systems, IEEE Transactions on*, 22(2):155–170, 2003.

[53] J. Richards and X. Jia. *Remote sensing digital image analysis: an introduction*. Springer Verlag, 2006.

[54] C. W. Rowley. Model reduction for fluids using balanced proper orthogonal decomposition. *International Journal of Bifurcation and Chaos*, 15:997–1013, 2005.

[55] C. W. Rowley, T. Colonius, and R. M. Murray. Model reduction for compressible flows using pod and galerkin projection. *Physica D: Nonlinear Phenomena*, 189:115–129, 2004.

[56] C. W. Rowley, I. Mezic, S. Bagheri, P. Schlatter, and D. S. Henningson. Spectral analysis of nonlinear flows. *Journal of Fluid Mechanics*, 641:115–127, December 2009.

[57] W. Rugh. *Linear system theory*. Prentice-Hall, Inc., 1996.

[58] M. Schetzen. *The Volterra and Wiener Theories of Nonlinear Systems*. New York: Wiley, 1980.

[59] W. Schilders, H. Van Der Vorst, and J. Rommes. *Model Order Reduction: Theory, Research Aspects and Applications*. Mathematics in Industry. Springer, 2008.

[60] K. Schittkowski. Nlpql: A fortran subroutine solving constrained nonlinear programming problems. *Annals of operations research*, 5(1):485–500, 1986.

[61] P. Schmid. Dynamic mode decomposition of numerical and experimental data. *Journal of Fluid Mechanics*, 656(1):5–28, 2010.

[62] P. N. Shankar and M. D. Deshpande. Fluid mechanics in the driven cavity. *Annual Review of Fluid Mechanics*, 32:93–136, 2000.

[63] W. Silva. Identification of nonlinear aeroelastic systems based on the volterra theory: Progress and opportunity. *Nonlinear Dynamics*, 39(1–2), 2005.

[64] S. Sirisup and G. Karniadakis. A spectral viscosity method for correcting the long-term behavior of pod models. *Journal of Computational Physics*, 194(1):92 – 116, 2004.

[65] S. Sirisup, G. E. Karniadakis, D. Xiu, and I. G. Kevrekidis. Equation-free/galerkin-free pod-assisted computation of incompressible flows. *Journal of Computational Physics*, 207(2):568 – 587, 2005.

[66] L. Sirovich. Turbulence and the dynamics of coherent structures, part I: Coherent structures. *Quarterly of Appl. Math.*, XLV:561–571, 1987.

[67] T. Smith, J. Moehlis, and P. Holmes. Low-dimensional modelling of turbulence using the proper orthogonal decomposition: A tutorial. *Nonlinear Dynamics*, 41(1-3):275–307, Aug. 2005.

[68] D. Sorensen and A. Antoulas. The sylvester equation and approximate balanced reduction. *Linear Algebra and its Applications*, 351:671–700, 2002.

[69] G. Tadmor, O. Lehmann, B. Noack, L. Cordier, J. Delville, and M. Bonnet, J.P. andA. Morzynski. Reduced order models for closed-loop wake control. *Philosophical Transactions of the Royal Society A*, 369:1513–1523, 2011.

[70] F. Terragni, E. Valero, and J. M. Vega. Local pod plus galerkin projection in the unsteady lid-driven cavity problem. *SIAM Journal on Scientific Computing*, 33(6):3538–3561, 2011.

[71] L. Trefethen. *Spectral methods in MATLAB*, volume 10. Society for Industrial Mathematics, 2000.

[72] L. Ukeiley, L. Cordier, R. Manceau, J. Delville, M. Glauser, and J. Bonnet. Examination of large-scale structures in a turbulent plane mixing layer. part 2. dynamical systems model. *Journal of Fluid Mechanics*, 441(1):67–108, 2001.

[73] R. Vaccaro. *SVD and Signal Processing II: Algorithms, analysis and applications*. Elsevier Science Inc., 1991.

[74] M. Wall, A. Rechtsteiner, and L. Rocha. Singular value decomposition and principal component analysis. *A practical approach to microarray data analysis*, pages 91–109, 2003.

[75] Z. Wang, I. Akhtar, J. Borggaard, and T. Iliescu. Two-level discretizations of nonlinear closure models for proper orthogonal decomposition. *Journal of Computational Physics*, 230(1):126 – 146, 2011.

[76] M. Wei. *Jet noise control by adjoint-based optimization*. PhD thesis, 2004.

[77] P. Welch. The use of fast fourier transform for the estimation of power spectra: a method based on time averaging over short, modified periodograms. *Audio and Electroacoustics, IEEE Transactions on*, 15(2):70–73, 1967.

[78] K. Willcox and J. Peraire. Balanced model reduction via the proper orthogonal decomposition. *AIAA Journal*, pages 2323–2330, 2002.

[79] K. Zhou, J. Doyle, and K. Glover. *Robust and Optimal Control*. Prentice Hall, 1996.

Biography

Maciej Balajewicz was born in Gliwice, Poland on Oct, 4, 1980. He graduated from Father Michael Goetz Secondary School in Ontario, Canada in 1999. He earned his Bachelors of Engineering from Carleton University in Ottawa, Canada in 2004 and his Masters of Applied Science from Carleton University in 2007.